Design of Biomimetic Armor Based on Strain Rate Sensitive Natural Dermal Armor

Sean S. Ghods

A thesis

submitted in partial fulfillment of the

requirements for the degree of

Master of Science

University of Washington

2018

Committee:

Dwayne Arola

Marco Salviato

Junlan Wang

George Mayer

Program Authorized to Offer Degree:

Department of Materials Science and Engineering

University of Washington

Abstract

Design of Biomimetic Armor Based on Strain Rate Sensitive Natural Dermal Armor

Sean S. Ghods

Chair of the Supervisory Committee:

Professor Dwayne Arola
Department of Materials Science and Engineering

Elasmoid fish scales serve as a dermal armor and are a marvelous example of a biological composite in Nature that exhibits exceptional mechanical behavior. Their hierarchical microstructure consists of two distinct and primary regions across the thickness. The outermost layer is known as the limiting layer (LL) and consists of calcium deficient apatite and discrete, sparsely distributed collagen fibers. The second layer is the elasmodine and consists of lamella of uniaxially aligned collagen fibrils with significantly lower mineral content. As collagen is the major constituent of fish scales, they would be expected to exhibit a high degree of strain rate sensitivity. Therefore, an experimental evaluation of the strain rate sensitivity of elasmodine fish scales was conducted in uniaxial tension and transverse puncture loading arrangements. It is shown that across a broad range of strain rates in tension, from 10^{-4} to 10^{2} s^{-1}, and ramp rates in transverse puncture, from 0.05 to 50 mm/s, the scales have an exponent for the toughness of 0.10 and 0.35, respectively.

The mechanics of collagen depend heavily on intermolecular bonding. Based on their high collagen content, hydrogen bonding can extend across fibrils and interfaces of the lamellae. Thus, a polar solvent (ethanol) was introduced to scales to change the interface bonding and evaluate its effects on the scale's mechanical behavior. In addition to the strain rate sensitivity, exposure of the scales to ethanol invoked significant increases in the elastic modulus, strength, and toughness across all loading rates. The largest increase noted was a 7X increase in the work to failure for transverse puncture loading.

In an effort to apply these findings towards the development of new armors, novel "first-generation" composites were developed with features of the fish scale microstructure. Specifically, fibrous ultra-high molecular weight polyethylene composites were fabricated using Dyneema as a platform and reinforced selectively with alumina particles. The experimental materials were evaluated in the same transverse puncture loading format. The addition of alumina powder to the polymer fiber composite resulted in increases across the performance metrics measured, but not yet to the level achieved by the scales. These results show promise and merit further investigation in the development of composites that draw inspiration from natural dermal armor.

TABLE OF CONTENTS

LIST OF FIGURES

ACKNOWLEDGEMENTS

First, I would like to thank Dr. Dwayne Arola for all of the guidance and encouragement to pursue the thesis option for the Masters of Science. Without him I would not have completed this rewarding research. As an advisor, he was always motivated towards this goal and I am greatly appreciative of his dedication to my success. Also, I want to thank all the other members of my defense committee; Dr. Junlan Wang and Dr. Marco Salviato. A special acknowledgement goes to Dr. Malakoutian for recommending me to the Dept. of Aeronautics and Astronautics here at the University of Washington to receive a Teaching Assistantship. This position provided me the funding to continue the pursuit of this degree. I also want to thank Michelle Hickner and Bill Kuykendall for their training on the equipment that allowed for much of the analysis in this thesis. Finally, I want to thank my friends and family for always being there and supporting me regardless of the path I choose.

Chapter 1. INTRODUCTION

Human skin is a remarkable impermeable barrier that prevents ingress of many harmful substances. However, it is not designed for protection against many forms of physical contact. Specifically, it underperforms in abrasion and transverse concentrated loading when compared to most engineering materials. In fact, there are many scenarios in which human skin is not a sufficient form of protection. Armors have been developed to add an external layer to the skin for improved protection against external physical threats. These armors can range from simple plastic layers for improved puncture resistance to ceramic plates that are enrolled for ballistic protection. At present, there is general belief that the existing material candidates for ballistic applications has matured and stagnated [Williams, 2017]. In search of improved material systems, it is prudent to take inspiration from novel materials and structures where opportunity arises.

Millions of years of natural evolution has resulted in a wide range of dermal armors. Researchers have investigated several of these armor systems for characterization of the microstructures and mechanical properties. This thesis expands upon the mechanical characterization of a selected natural dermal armor and lays some groundwork for the development of biomimetic composite armors that are inspired by this natural material.

1.1 MODERN ARMOR SYSTEMS

Armor development has not advanced to the same degree that weapons have. Body armor started out as simple thick leather layers [Larsen et al., 2011; Peleg et al., 2006]. It progressed to metal plate and chainmail armors as the ability to produce metals occurred. With progression into the modern era and firearms were developed, it was clear that traditional metal or leather armor were not sufficient [David et al., 2009]. Concurrently, new armors must remain resistant to lower

velocity punctures that result from sharp-edged weapons since that is still a relevant form of attack. These new armors tend to be woven, high toughness, polymer fiber vests made of ultra-high-molecular-weight polyethylene (UHMW-PE) or Kevlar. They are fairly puncture resistant but require a significant number of layers to be effective, which can lower the flexibility of the material system. To further improve the resistance to bullet impacts and explosives, the vest can include a high strength metal (mainly steel, but sometimes titanium), technical ceramic (boron or silicon carbide), or a composite of ceramic and fiber backing. These plate inserts are inflexible, which reduces the mobility of the individual that bears them. Examples of these forms of ballistics protection can be seen in Figure 1.1.

Figure 1.1. Examples of ballistic protection materials post-impact. Left: woven polyaramid fiber vest after impact by multiple small caliber (pistol) bullets. Middle: high strength steel plate that withstood many more impacts. Right: CT image of a boron carbide composite plate with three points of impact [Wells, 2008].

Each of the aforementioned materials used for protection have their own relative advantages over the others. Unconsolidated woven polymer vests are tough, low density, and flexible. Flexibility comes from the fabric nature of the material. The fibers can buckle under low speed bending without compromising the integrity of the polymer. High strength steel plates are a

middle ground for armors in terms of protection. These armors are extremely tough, high density, and stiff. Because of their properties, steel plates can protect against multiple impacts, but at the cost/penalty of increased weight and reduced flexibility. Ceramic plates have a density between that of the polymer and steel. Because of their strength and high hardness, they provide the best protection against singular high velocity impacts. However, due to their brittleness, they undergo brittle fracture after impact and their integrity is severely compromised; that reduces their capacity to provide protection against further impacts.

Composite panels are an attempt to mitigate the low toughness of monolithic ceramic plate armors. They typically consist of a ceramic plate that is adhered to a polymeric fiber composite. When impacted, the ceramic will absorb the brunt of the kinetic energy and dissipate it across the plate through fracture. Backing it with the composite allows the ceramic to fracture in a less catastrophic fashion and retain more of its intrinsic structural integrity. Impact resistance will be compromised to a lesser degree than a ceramic without backing, allowing for multiple impacts of lower kinetic energy. These material systems achieve greater impact resistance but are still plagued by the issue of high weight and inflexibility. Polymeric fabrics are the lightest and most flexible but those have other issues limiting them.

1.2 Natural Dermal Armor

In Nature there is prey and predator. Predators are fast and strong, which enables them to catch and over-power their prey. They have sharp teeth, claws, and talons to kill and consume their prey. Prey protect themselves from predatory attacks through a variety of methods, including camouflage, evasion with greater speed, and other traits that allow the prey to avoid capture. One of the most common forms of defense is body protection. Many animals that are under threat from

predators have developed dermal armor that is meant to protect against an array of attacks. Some animals have hard, relatively inflexible armor like the armadillo and others have tough, flexible armor like fish [Yang et al., 2013. The difference between these armors, in the case of fish v. armadillo, is akin to the difference in mechanical properties of polymeric fiber and ceramic plate ballistics armors.

A number of important studies have been performed on the armor of armadillos, alligators, crocodiles, turtles, and fish [Chen et al., 2011; Archrai and Wagner, 2013; Sun and Chen, 2013; Chen et al., 2014; Chen et al., 2015; Chang and Chen, 2016; Ikoma et al., 2003; Ortiz and Boyce, 2008; Torres et al., 2008; Lin et al., 2011]. Each of these animals has a unique form of armor. Materials for these systems are similar, consisting of the typical structural polymers (polypeptides and polysaccharides) and minerals (apatite) found in most biological systems. In all research performed on natural dermal armor, the materials are found to have a hierarchical structure [Wengst et al., 2014]. The combination of organic and inorganic substances in the various hierarchical structures are essential in tailoring the materials to achieve properties that are optimized for the particular animal's environment.

The armors of many animals consist of a hard, bony material that is capable of preventing puncture, but is stiff. As such, reduced flexibility is a relevant issue with some natural dermal armors. Structural design is used for these systems to overcome the stiffness of the actual armor. For example, armadillos utilize an assembly of bony materials, interconnected with fibrous collagen to hold everything together [Yang et al., 2012]. In comparison, pangolins rely on keratinous scales that are curved and overlapping to allow for locomotion, but at reduced levels of protection [Wang et al., 2016; Liu et al., 2016]. Elasmoid fish scales are similar to the protective "scales" of the pangolin as they are arranged in an overlapping pattern, but they consist of different

materials and microstructure. Locomotion for fish is achieved by contortion of the body, which is opposed to the pedal motion for terrestrial animals. As such, the flexibility for many fish is of prime importance to allow fast swimming and evasion of predators.

1.3 Fish Scales

The ideal armors would possess puncture resistance, be capable of dissipating large amounts of energy through deformation or new surface area, and remain reasonably light and flexible. Within the last decade, scientists have started to explore the viable options in Nature for new and innovative solutions [Bruet et al., 2008]. Carnivorous animals need to kill other animals for survival. As a result, some prey have developed natural armors. With hundreds of millions of years of evolution, their armors have been slowly refined to be more effective. Fish are particularly interesting since they have a type of protection that must be flexible enough to not encumber the mechanics of locomotion. Fish with elasmodine scales achieve protection through a distribution of discrete scales that are arranged in an overlaying pattern (Figure 1.2a). The flexibility required by the fish is possible from the overlaying pattern, as well as from the limited thickness of the individual scales.

Figure 1.2. Elasmodine scales of an east asian carp. a) assembly of scales over the body of a fish, b) photograph of a carp scale being folded over, demonstrating a high degree of flexibility. All mechanical properties are maintained when returned to its neutral, unflexed state.

Fish scales can be categorized in many ways. The shapes of scales are typically categorized into four major types, including placoid, ganoid, cycloid, and ctenoid [Sudo et al., 2002]. The structure of scales are categorized as placoid, ganoid, cosmoid, and elasmoid [Sire et al., 2003; Kardonget al., 2006]. Placoid, ganoid, and cosmoid scales are thick and stiff bony scales, which rely on the integrated pattern of the scales for flexibility. Elasmoid scales facilitate flexibility beyond just articulation by their limited thickness and material microstructure.

A number of scientists have initiated investigations into the structure and properties of fish scales from a variety of species. The scales of several fish have been studied, including the Arapaima gigas, Pagrus major, Cyprinus carpio, etc. [Lin et al., 2011; Torres et al., 2008; Ikoma et al., 2003; Zhu et al., 2013; Garrano et al., 2012]. In general, these studies have included microstructural analyses and experimental evaluations of the mechanical properties. The recent evaluations of Murcia, [2017] have included a variety of novel concerns such as temperature ranges, chemical environments, hydration states, etc. In addition to their exceptional mechanical behavior, one of the most exciting aspects of elasmodine scales is their microstructure, as seen in Figure 1.3. Elasmodine scales are a laminated composite consisting of collagen fibers and apatite. The outer layer of the scale is regarded as the limiting layer (LL) and is a highly-mineralized matrix of apatite reinforced by a sparse distribution of type I collagen fibrils [Garrano et al., 2012]. Beneath the LL is the elasmodine, which consists of an assembly of lamina (or plies) of unidirectional type I collagen fibrils and is divided into two additional layers. The external elasmodine (EE) lies beneath the LL and consists of a series of relatively heavily mineralized collagen fiber layers [Murcia, 2017]. Residing beneath the EE is the internal elasmodine (IE)

which has the same basic structure as the EE, but significantly less mineral. The collagen fiber plies within the entire elasmodine follow a Bouligand stacking sequence which means each layer is oriented at an angle less than 90 degrees with respect to the former, and thus forming a helical stack [Murcia et al., 2017].

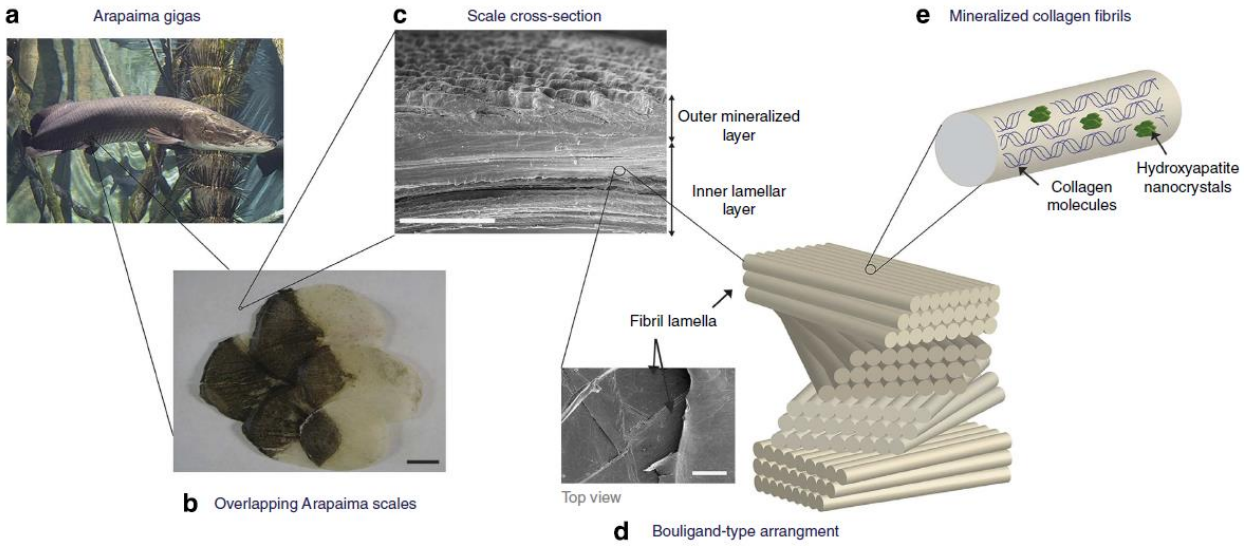

Figure 1.3. Schematic of the hierarchical structure that exists in fish scales. The scales from an Arapaima gigas have a layered structure with the outer layers being heavily mineralized collagen fiber matrix and the mineralization decreases progressing inward. The collagen fibers consist of bundles of fibrils that are groups of aligned, mineralized tropocollagen fibrils. [Zimmerman et al., 2013].

1.4 COLLAGEN TYPE I

Elasmodine scales exhibit a bouligand composite structure and consist primarily of mineralized collagen fibers. Collagen fibers have a hierarchical structure that consists of bundles of fibrils, that are broken down further into overlapping aligned tropocollagen molecules. Tropocollagen is a triple helix of polypeptide chains that are typically made of glycine (Gly), proline (Pro), and hydroxyproline (Hyp) amino acids. Figure 1.4 is a schematic diagram of a type I collagen fibril and the aforementioned hierarchical arrangement.

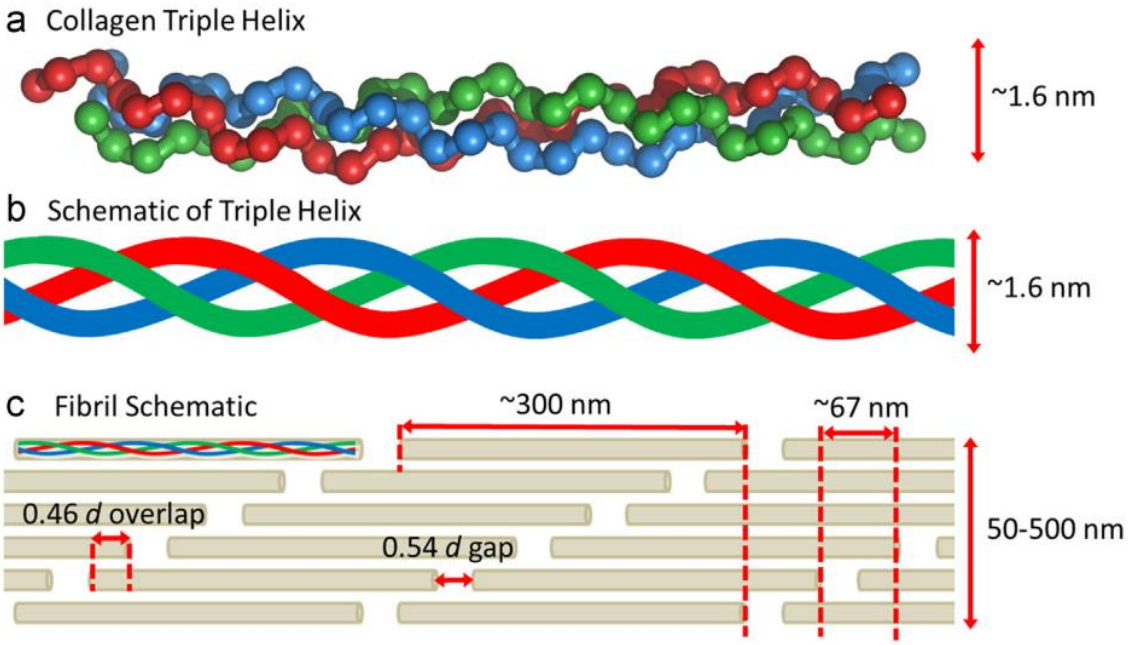

Figure 1.4. The structure of collagen. a) Molecular model of tropocollagen. b) Schematic of the tropocollagen. c) Schematic of a collagen fibril [Sherman et al., 2015].

The dimensions of the fibrils in Figure 1.4 are generalized and can vary from fibril to fibril and from biological system to system. Variations can be brought about from enzymes creating different lengths of tropocollagen from the pro-collagen chains. Length differences will cause different overlaps and kinks in the fibrils, where there is little overlap. In addition, the schematic diagram in Figure 1.4c shows the fibril with only a few triple helices bundled together. Yet, based on the diameter of fibrils there can be 30 – 300 tropocollagen chains across it. Tens of thousands of tropocollagen can be in a single fibril's cross section.

An additional schematic of the tropocollagen molecular arrangement of collagen fibrils is shown in Figure 1.5a. As seen in this figure, the polymer chains have dipoles on the amide and carboxyl groups. These dipoles will undergo weak bonding with others that are near. The closest dipoles would be those present on other chains or across the tropocollagen. It is possible for the external tropocollagen of one fibril to weakly bond to adjacent tropocollagens on other fibrils and

even fiber to fiber (Fig. 1.5b). When the chains are aligned, there is a significant amount of hydrogen bonding between them and other tropocollagen. But this bonding is present only in a dehydrated state. In the presence of water (Fig. 1.5c), the water molecules will interpenetrate the amino acid chains and disrupt the hydrogen bonding between and within the molecules in favor of hydrogen bonding with water molecules because of its high polarity. This will allow a greater degree of mobility between the chains and fibrils, which in turn allows larger deformations in the bulk fiber before failure.

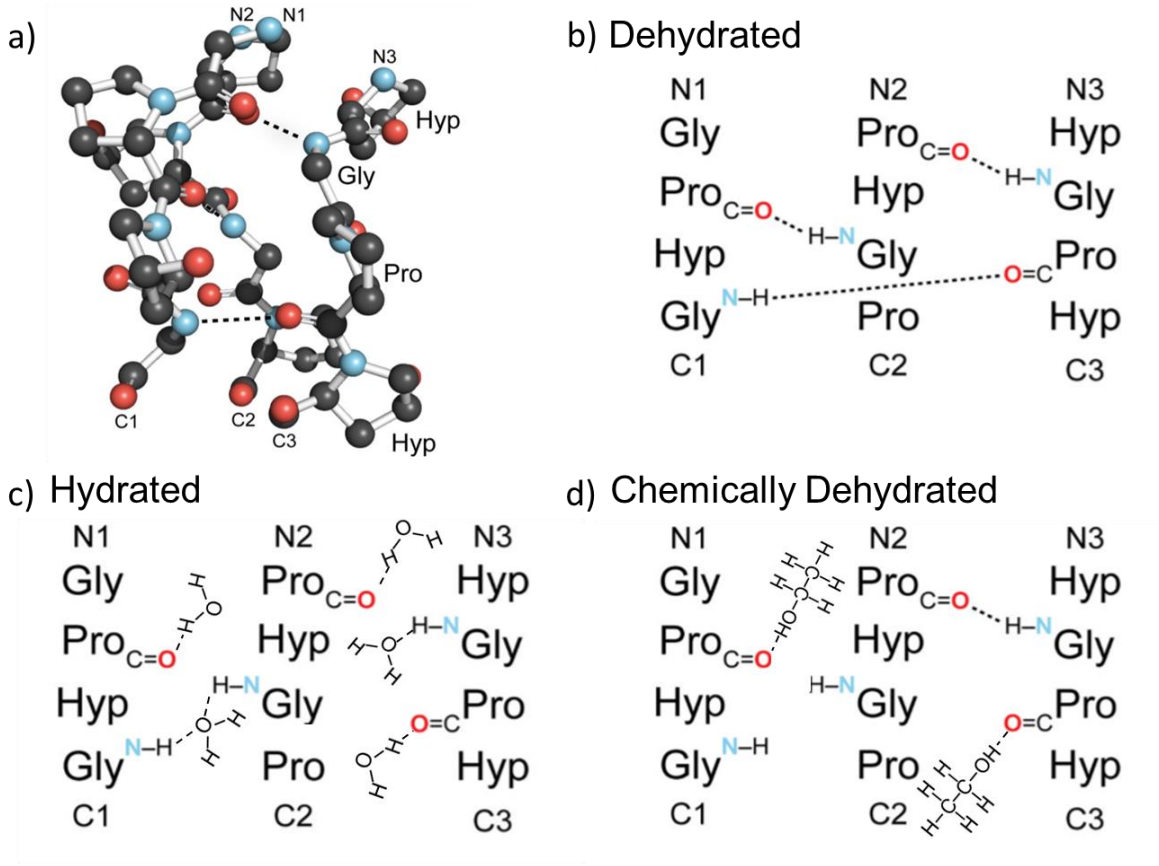

Figure 1.5. The molecular and protein structure of collagen. a) 3D schematic segment of tropocollagen of glycine (Gly), proline (Pro), and hydroxyproline (Hyp) in a dehydrated state with carbon as black, oxygen as red, nitrogen as blue, and hydrogen not shown. The dotted lines indicate hydrogen bonding. b) planar schematic of a dehydrated tropocollagen segment with polypeptides aligned instead of in the triple helix configuration. c) Schematic of a hydrated

tropocollagen segment with water molecules penetrating the helix and disrupting interpeptide hydrogen bonding. d) Schematic tropocollagen segment chemically dehydrated with ethanol. Lower polarity that water will facilitate some interpeptide bonding. Adapted from Shoulders et al. [2009].

There are mechanical benefits and drawbacks for both the hydrated and dehydrated states of collagen with respect to their potential performance as flexible armors. Water increases the compliance and strain to failure of collagen-based tissues, but causes the collagen to be weaker and less stiff. This combination would lower the resilience of the fibers overall. Dehydration by free convection would cause the opposite, i.e. lower the energy absorption in the plastic regime and lower toughness because of less chain sliding prior to failure. Interestingly, this is where chemical dehydration would be expected to be advantageous. If a polar solvent is introduced that has a lower Hoy's solubility parameter than water, it will displace the water molecules and allow secondary bonding between the collagen peptides, but within a liquid environment. The lower strength of the hydrogen bonds to the polar solvent allows the bonds to break and flow of the solvent and chains around it. In theory, this could cause an increase in strength and stiffness due to the interpeptide bonding with respect to the hydrated state, but without a substantial loss of strain to failure. Overall, the polar solvent treatment should result in higher toughness for collagen-based tissues when compared to the hydrated state. However, this should be dependent on the level of inter-and extra-fibrillar mineral as that could interfere with the interpeptide bonding. Improvements to the elastic modulus, strength, and toughness of carp scales by chemical dehydration have already been demonstrated in the literature [Murcia et al., 2016]. However, this prior evaluation was performed at a single and low strain rate. It is unknown how this mechanism of toughening will extend to dynamic loading.

The mechanical response of collagen fibrils is dependent on its hierarchical structure. Some

groups have characterized individual collagen fibers and models have been proposed to explain the mechanics of collagen [Buehler, 2007; Depalle et al., 2015; Fratzl et al., 1997; Nagai et al., 2004; Sankar et al., 2007; Sherman et al., 2015; Shoulders et al., 2009]. Figure 1.6 shows a mechanistic model that was been developed to help characterize the deformation of collagen fibrils loaded in tension proposed by Depalle et al., [2015].

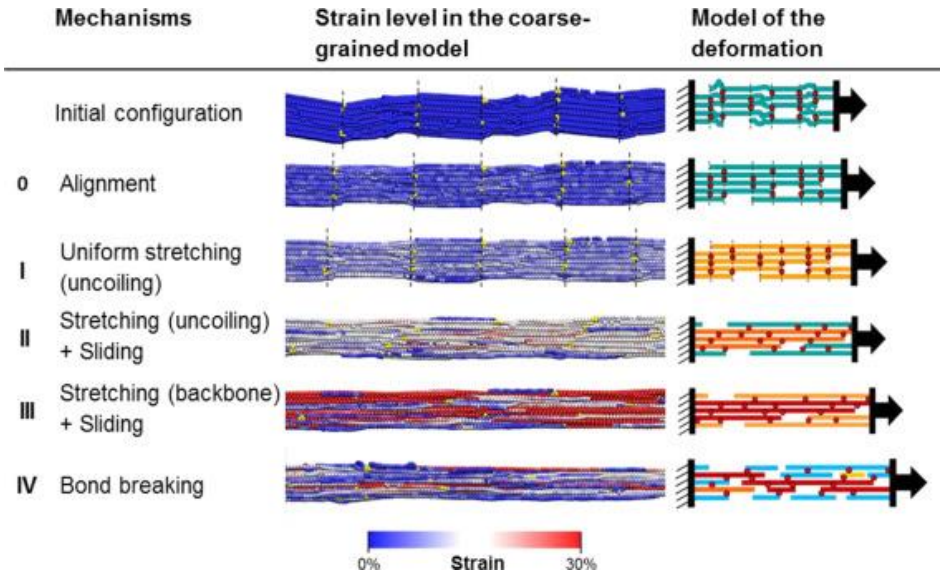

Figure 1.6. Deformation model for a type I collagen fibril with some covalent intermolecular bonding under uniaxial tension. [Depalle et al, 2015]

According to the model of Depalle et al. [2015], the deformation of collagen begins in a kinked and slightly compressed state. Once loading commences, the fibrils decompress and the chains of the tropocollagen align with the loading axis. Then the triple helixes will begin to uncoil with the chains undergoing stretching in the loading direction. The tropocollagen will continue to unravel, while some of the tropocollagen molecules will begin to slide against each other. Then, the chains of each triple helix (which now don't necessarily form a true helix) will begin to slide. Finally, the maximum amount of deformation is achieved from the uncoiling and

slippage between the chains, so that the energy from the loading causes failure of intermolecular covalent bonds [Buehler, 2007; Depalle et al., 2015; Fratzl et al., 1997; Sherman et al., 2015].

The model by Depalle et al. [2015] can be partially extrapolated to consider a chemically dehydrated collagen system where there is no secondary intermolecular bonding involving water molecules, but instead a high number of weak intermolecular hydrogen bonds between dipoles of the proteins. In the first few steps of the loading, a lower degree of deformation would be expected since the energy will be used to break the weak secondary bonds. Depending on the time scale of the deformation, the polar solvent will act as a lubricant so the tropocollagen and peptide chains can slide more easily and potentially form additional secondary bonds amongst adjacent dipoles. The reformation of secondary bonds during the sliding will further dissipate energy and increase the load needed to elongate the fibrils. Of course, an evaluation of the rate dependence in the deformation behavior is needed to support this proposed behavior.

1.5 Motivation for Biomimetic Armors

Fish scales possess high specific strength and toughness, while also exhibiting a high degree of flexibility [Ikoma et al., 2003; Garrano et al., 2012; Murcia et al., 2015; Yang et al., 2014]. To improve upon the existing forms of personal body armor for providing protection from physical threats, it is logical to draw some inspiration from the microstructures that Nature has spent millions of years developing and refining. The unique hierarchical composite structure of elasmoid scales have not been mimicked using common engineering materials. It may be possible to develop armors that vastly outperform those that are presently in use via mimicking the natural armors with appropriate synthetic materials.

In general, there are two distinct ways for elasmoid fish scales to serve in the biomimetic

development of new armors. The first consists of engineering a material system to possess a scale distribution over and across the surface of the body to be protected. This effort consists of optimizing the overlap, size of scales, shape, etc. to obtain the ideal compliancy of the entire system without focusing the microstructure and mechanical properties of the scales. This is a mechanical design problem and can be maximized for any material. Indeed, some groups have explored and modelled scale systems to determine promise of scale patterning [Browning et al., 2013; Vernerey et al., 2010; Venerey et al., 2014]. The second aspect of biomimetic guided design is to produce a material that mimics the microstructure of the scales themselves to achieve a substantial improvement in mechanical properties. This is a materials problem.

There are many aspects of the scale that can be emulated with engineering materials, some of which is more difficult than others. The rotational angle of the lamina does not conform to the standard 0°, 90°, ±45° orientations used in most commercial continuous fiber composites [Murcia et al., 2017]. Intermediate angles may perform better for armor applications and puncture resistance, and could be investigated [Yang et al., 2014]. Material selection for the matrix and fibers to match those of scales would entail a high toughness polymeric fiber with addition of ceramic-based particulate reinforcement to the matrix. Stacking of different composites could be used to imitate the drastic variations in mineral content through the thickness of the elasmodine. In addition, an etched ceramic could be used for the LL if designed to conform to the sawtooth patterning found in the scales. These are all worthy options, but require a greater understanding of the scale performance under dynamic loading, and the importance of the microstructure.

The remainder of this thesis describes experimental studies focused on further understanding the structure and strain rate sensitivity of elasmodine fish scales, as well as investigating the potential benefits of using this material to guide the development of new flexible

armors. In Chapter 2, experimental studies are described involving scales of the east Asian carp and evaluations of the strain rate sensitivity by uniaxial tension and transverse puncture. In Chapter 3, an evaluation of the strain rate sensitivity is conducted after treatment of carp scales using a polar solvent. Then in Chapter 4, new hybrid materials are developed using a commercial fibrous UHMW-PE material that is reinforced with alumina particles. The performance is evaluated in terms of the transverse puncture resistance and mechanisms of failure. The thesis then presents conclusions of the work in its entirety and offers some ideas for future work.

Chapter 2. MECHANICAL RESPONSE OF CYPRINUS CARPIO IN UNIAXIAL AND TRANSVERSE LOADING

2.1 SYNOPSIS

Natural dermal armors are serving as a source of inspiration in the pursuit of "next-generation" structural materials. Although the dynamic strain response of these materials is arguably the most relevant to their performance as armors, limited work has been performed in this area. Here, uniaxial tension and transverse puncture tests were performed on specimens obtained from the scales of Asian carp over strain rates spanning seven decades, from 10^{-4} to 10^{3} s^{-1}. The importance of anatomical variations was explored by comparing the performance of scales from the head, middle and tail regions. In both loading orientations, the scales exhibited a significant increase in the resistance to failure with loading rate. The rate sensitivity was substantially higher for transverse loading than for in-plane tension, with average strain rate sensitivity exponents for measures of the toughness of 0.35 and 0.10, respectively. Spatial variations in the properties were largest in the puncture responses, and scales from the head region exhibited the greatest resistance to puncture overall. The results suggest that the layered microstructure of fish scales is most effective at resisting puncture, rather than in-plane tension, and its effectiveness increases with rate of loading. Understanding the contributions from the microstructure to this behavior could be key to the development of flexible engineered laminates for penetration resistance and other related applications.

2.2 INTRODUCTION

Fueled largely by the pursuit to develop "next generation" structural materials, interest in the science of natural materials has been quickly growing [Barthelat, 2012; Meyers et al., 2011]. One

category of materials that has attracted substantial interest is natural dermal armors [Yang et al., 2013]. These materials are charged with providing protection against physical threats, and are subjected to the most extreme loading conditions. The dermal armors of armadillo [Chen et al., 2011], alligators and crocodiles [Acrhrai and Wagner, 2013; Sun and Chen, 2013; Chen et al., 2014], turtles [Chen et al., 2015; Chang and Chen, 2016], and fish [Ikoma et al., 2003; Ortiz and Boyce, 2008; Torres et al., 2008; Lin et al., 2011] are just a few examples of the materials being explored in this area. Based on their morphology, the armors of the aforementioned animals appear unique, but all are biological composites composed of organic and inorganic building blocks that are organized with a hierarchical structure [Wegst et al., 2014]. What potentially sets these armors apart from one another is the organization of the constituents into specific structural elements at larger length scales, that essentially tune the mechanical behavior [Naleway et al., 2015].

Fish scales are of particular interest in the most recent pursuits to develop bioinspired materials [Browning et al., 2013; Zhu et al., 2013; Chintapalli et al., 2014; Rudyk et al., 2015; Martini and Barthelat, 2016]. The scales in modern fish have evolved into four primary groups including cosmoid, placoid, ganoid and elasmoid scales [Sire and Huysseune, 2003; Kardong, 2006]. Cosmoid, ganoid and placoid scales are all relatively rigid in comparison to elasmoid scales, which results from their larger thickness and the presence of bony regions with much higher mineral content [Sherman et al., 2017]. Flexibility in these dermal armors is achieved by the way the scales articulate with respect to one another, rather than the flexibility of the scales themselves. In comparison, elasmoid scales are much thinner, and are stacked or overlayed with respect to one another to facilitate flexibility and protection simultaneously. Elasmoid scales are characteristic of fish with greater speed, and could be considered more multi-functional as their

flexibility appears to be equally important to the puncture resistance [Bruet et al., 2008; Jandt, 2008].

The primary building blocks of elasmoid scales are apatite and type I collagen fibers [Lin et al., 2011; Garrano et al., 2012; Zhu et al., 2012; Gil-Duran et al., 2016]. The microstructure of these scales is often described as consisting of two layers, including a thin outermost highly mineralized layer, and the elasmodine layer, which occupies the bulk of the scale thickness. The outermost layer, known as the Limiting Layer (LL), is a highly mineralized matrix of calcium-deficient apatite crystals reinforced by a sparse dispersion of thin collagen fibers [Zylberg 1982]. The elasmodine consists of a number of lamina (or plies) of unidirectional type I collagen fibrils. Closer scrutiny shows that the elasmodine actually consists of two discrete layers [Murcia, et al., 2015] that are distinguished by the relative mineral content (Figure 2.1a). The internal elasmodine (IE) consists of discrete plies of unidirectional collagen fibers with little to no mineral reinforcement. The external elasmodine (EE) exhibits higher mineral content than the IE, but far less than the LL [Murcia et al., 2016]. The plies of the entire elasmodine are arranged in the form of a plywood structure, with rotation between plies ranging between 60–90° depending of the fish [Bigi, 2002]. For the carp, the average angle of rotation between plies is 75° [Murcia et al., 2017a].

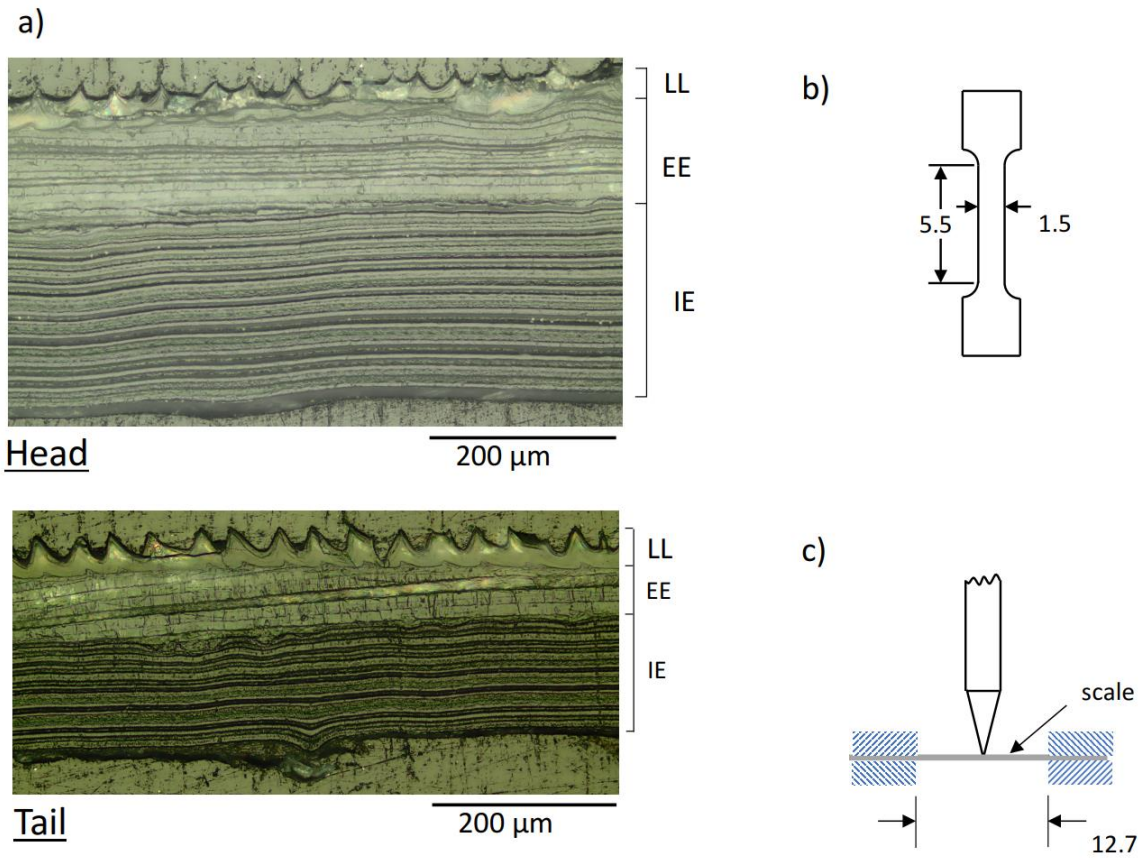

Figure 2.1. Details of the scales and the experimental methods adopted for evaluating the dynamic behavior. a) carp scale cross-sections for representative head and tail scales. The three principal layers are highlighted including the limiting layer (LL), external elasmodine (EE) and internal elasmodine (IE), b) tensile testing, b) puncture testing. All units are in millimeters.

The strong mineral gradient across the thickness of elasmoid scales results in distinct spatial variations in the hardness and elastic modulus. From the limiting layer to the internal elasmodine there is a reduction in elastic modulus and hardness [Lin et al., 2011], which reportedly plays an important role on the puncture resistance [Zhu et al., 2012]. Due to the high mineral content, the LL dissipates energy by brittle fracture. The failure process continues to the EE, which results in delamination at the LL/EE interface, as well as between adjacent plies. Once

the LL and EE have undergone gross failure, further penetration is resisted by stretching of the fibrils of the IE, as well as rotation and delamination along the interface of the collagen plies [Zimmerman et al., 2013; Yang et al., 2015]. The combination of delamination, rotation of the plies and inelastic deformation of the individual lamina provides the scales with incredible notch insensitivity [Khayer and Barthelat, 2015] and resistance to fracture [Yang et al., 2014; Murcia et al., 2016]. Due to its composition the and aforementioned mechanisms of deformation, the IE contributes substantially to the toughness, and over a large range of temperatures [Murcia et al., 2017].

Flexible or "wearable" armor materials require low stiffness and high resistance to puncture. As a consequence, the puncture resistance of scales has received considerable attention [e.g. Zhu et al., 2011; Meyers et al., 2012; Allison et al., 2013; Zhu et al., 2013; Khayer Dastjerdi and Barthelat, 2015]. But while the dynamic response of these materials is one of the most relevant to their performance to resist attack, limited work has addressed the properties of scales under dynamic loading. In fact, only one study has performed an evaluation of the strain rate dependence of fish scale properties, which was performed in uniaxial tension [Lin et al., 2011]. Owing to the importance of interfaces in natural structural materials [Barthelat et al., 2016], and the different mechanisms they impart to the structural behavior, the strain rate dependence of scales and their resistance to failure could be quite different in the axial and transverse loading arrangements. The interfaces may contribute to the transmission of damage differently in transverse puncture and tension, simply by virtue of the stress state and the orientation of the principal components with respect to the interfaces.

In this investigation, an evaluation of the dynamic loading response of fish scales was conducted that involved uniaxial tension and transverse puncture to failure. The primary

objective of this study was to characterize the importance of the layered microstructure on the strain rate sensitivity of the deformation behavior and its orientation dependence.

2.3 Materials and Methods

Scales of the *Cyprinus carpio* (i.e. the common freshwater carp) were obtained by extraction from across the body of several fish. These fish were marketed as East Asian carp, and no additional information was available. The scales were obtained nearly equidistant between the ventral and dorsal aspects of the body (i.e. adjacent to the midline) and from three regions including near the head, mid-length (beneath the dorsal fin) and near the tail. To be consistent, these regions were defined at distances from the gill plate of approximately 15%, 40% and 80% of the total number of scales counted along the lateral line over the fish length. All of the scales were less than 1 mm thick and possessed a diameter that varied according to the anatomical position. After extraction, the scales were stored in Hanks Balanced Salt Solution (HBSS) at room temperature.

To support an evaluation of the tensile properties, conventional dog-bone shaped tensile specimens were sectioned from the scales using a punch and stamping process [Garanno et al., 2012]. A single specimen was stamped from the center region of each scale where the thickness is most uniform. The specimens possessed a gage section length and width of roughly 6 mm and 1.5 mm, respectively, as shown in Figure 2.1b. All of the specimens were obtained with alignment parallel to the fish length, for consistency, as scales from the head region can exhibit anisotropic behavior [Murcia et al., 2015]. After sectioning, the specimens were returned to the HBSS bath at room temperature.

Tensile testing of the hydrated fish scale specimens was performed to failure at room temperature. The loading was performed under displacement control using a commercial universal testing machine (Instron ElectroPuls E1000, MA) equipped with load cell having full-scale range of 250 N and load precision of 0.01%. Stroke rates were selected to obtain strain rates from $1x10^{-4}$ to $1x10^{2}$ s^{-1} in decades, which were estimated according to the specimen gage length. All specimens were tested to failure. Five specimens were evaluated for each strain rate and anatomical region (head, middle and tail), which resulted in 7 rates x 3 regions x 5 specimens = 105 total tests.

The elastic modulus (E), strength (S) and modulus of toughness (MOT) were determined from results of the tension tests at each rate using the engineering stress-strain definitions. The elastic modulus was determined using the tangent method for strains less than 1% and the strength was defined by the maximum stress realized by the sample. The modulus of toughness was calculated by integrating the area under the stress-strain curves as a function of strain until failure.

Puncture tests were conducted on specimens from the three anatomical regions using a sharp stainless steel punch with tip radius of curvature = 40 um and included angle of 30°). Loading was conducted using a universal testing machine (Model ELF 3300, BOSE, Eden Prairie, MN, USA) on scales clamped within a dedicated fixture at rates that ranged from $5x10^{-2}$ to 50 mm/s. The scales were unsupported and clamped around the periphery with exposed portion of 12.7 mm as shown in Figure 2.1c. With an average thickness of approximately 0.5 mm, and ignoring the out of plane deflection, the loading rates corresponded to effective strain rates of approximately $1x10^{-1}$ to $1x10^{3}$ s^{-1}. Of note, the actual strain rates for the puncture tests varied according to the scale thickness. In all testing the scales were arranged with limiting layer oriented towards the punch and the load and displacement were acquired at a rate of 4 kHz. The scale

performance was evaluated in terms of the maximum punch load as well as work to puncture, which was obtained by integrating the load load-line displacements to the point of maximum load. For both the tension and puncture loading formats, validation tests were performed using specimens prepared from a polycarbonate sheet of 0.38 mm thickness, which is comparable to that of the scales.

The microstructure of scales within each region of evaluation was examined using scanning electron microscopy (JEOL, Model JSM- 6010PLUS/LA, Peabody, MA). The samples were sputtered with Au/Pd and observed in secondary electron imaging mode. In addition, selected scales were evaluated after puncture testing using microCT scanning with a North Star Imaging X5000. For this effort, the scales were treated with a very light coating of diluted ethylene glycol after Ryou et al., [2013] to maintain the moisture content within the scale and to minimize any distortion related to dehydration during scanning. Scales were scanned from the head region and at the lowest and highest loading rates. The scans were performed using the following parameters; 50 kV, 1000 uA, 1 fps, step scan mode with 10 ms delay, 900 projections, and 2 frame average. Fixturing of the scales, source, and detector created a geometric zoom of about 50x and resolution of 3 um/pixel. Radiographs were treated using ef-X reconstruction software to obtain images of relevance for display.

2.4 RESULTS

Typical stress-strain diagrams resulting from the uniaxial tension tests are shown in Figure 2.2. A single response obtained from the scale of the tail region at a rate of $1x10^{-3}$ s^{-1} is shown in Fig. 2.2a. Illustrations of the elastic modulus, strength and modulus of toughness are shown for reference. These measures were used as metrics for characterizing the tensile responses of all the

scale samples tested. Representative responses obtained at a low, intermediate and high loading rate are in shown in Fig. 2.2b through 2.2d. These graphs include responses obtained for scales from each of three regions. As evident from a comparison of the responses at the three strain rates, there is an increase in the strength and the degree of inelastic deformation to failure with an increase in the loading rate.

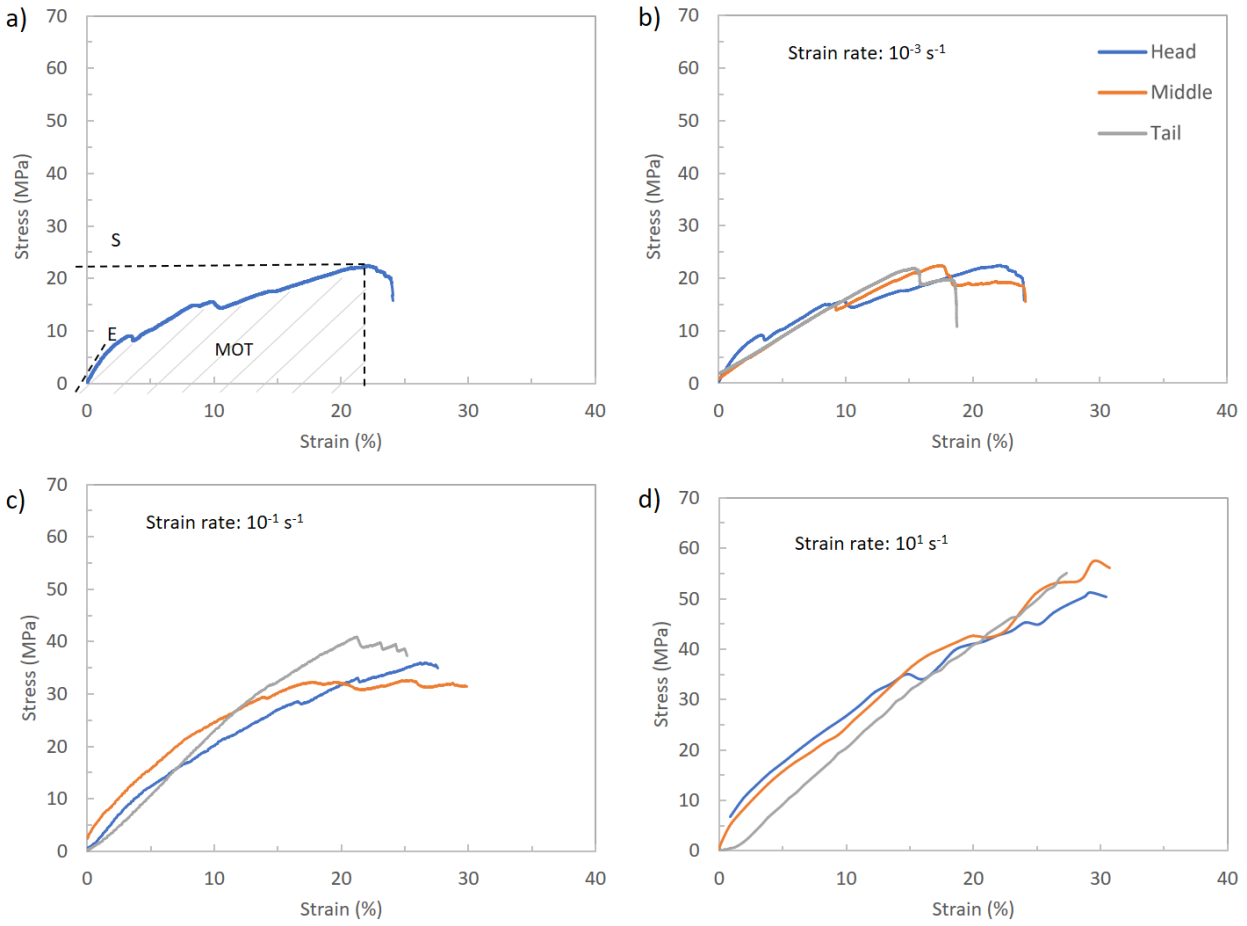

Figure 2.2. Representative stress-strain responses for scales from the three representative regions at three different strain rates. a) at 10^{-3} s^{-1}, b) at 10^{-1} s^{-1}, and c) at 10^{1} s^{-1}

The contribution of loading rate to the elastic modulus, strength, strain to failure and modulus of toughness of the scales is shown in Fig. 2.3a through 2.3d, respectively. Note that the data in each graph presents the average and standard deviation of responses obtained for the three

regions of evaluation, namely the head, middle and tail. Overall, there is an increase in all four properties describing the mechanical behavior with loading rate. However, the general trend in the property changes are not consistent. The elastic modulus underwent the largest increase in magnitude (up to 3X) over the range in strain rate as evident in Fig. 2.3a, whereas the smallest increase with loading rate was found in the strain to fracture, with less than 1.5X increase over the range of loading rate (Fig. 2.3c).

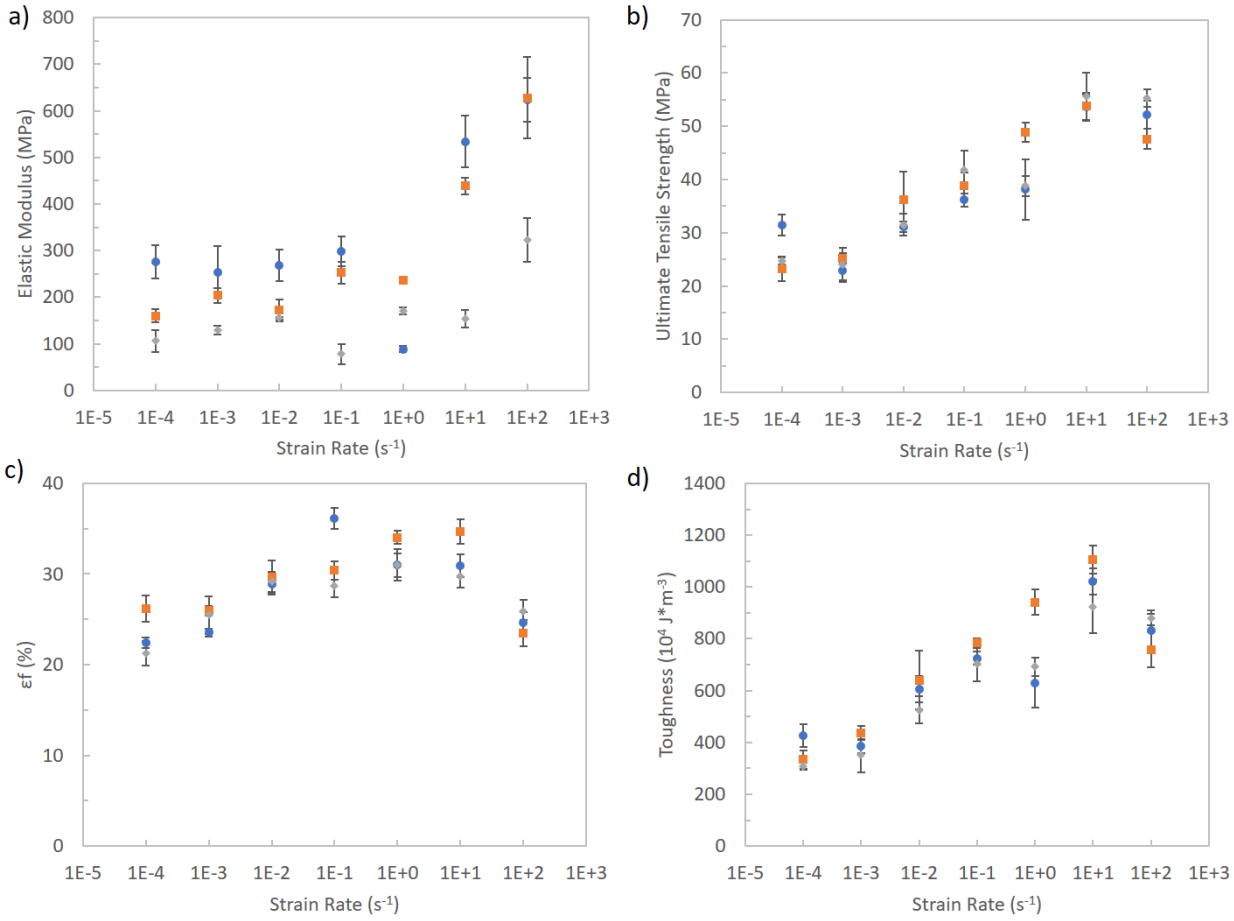

Figure 2.3. Strain rate dependence in the tensile responses of the scales for each of the three regions. (a) elastic modulus, (b) ultimate tensile strength, (c) strain at failure, and (d) modulus of toughness.

The strain rate sensitivity of the scales was interpreted from the measures of toughness for each of the three regions. While not a traditional property to evaluate the rate sensitivity, that

measure accounts for the changes in both the strength and the degree of inelastic deformation to failure. A simple power law response was used to characterize the responses, with a sensitivity exponent of m. In tension, the values of m for the head, middle and tail were 0.06, 0.07 and 0.08, respectively.

A representative load vs load-line displacement response for transverse loading to puncture of the scales is shown in Fig. 2.4a. Note that the stiffness, max load to puncture and corresponding work were used to quantify the mechanical behavior for this loading condition. Representative puncture responses for selected low, medium and high loading rates are shown in Fig. 2.4b through 2.4d, respectively; each of these graphs include typical responses for the three regions of evaluation as well as responses for the polycarbonate control. Consistent with the responses in tension, there was an increase in resistance to failure with increasing loading rate. However, in contrast to the increase in extensibility of the scales with loading rate in tension, the deformation to puncture decreases with loading rate as evident from comparing the responses from Fig. 2.4b through 2.4d.

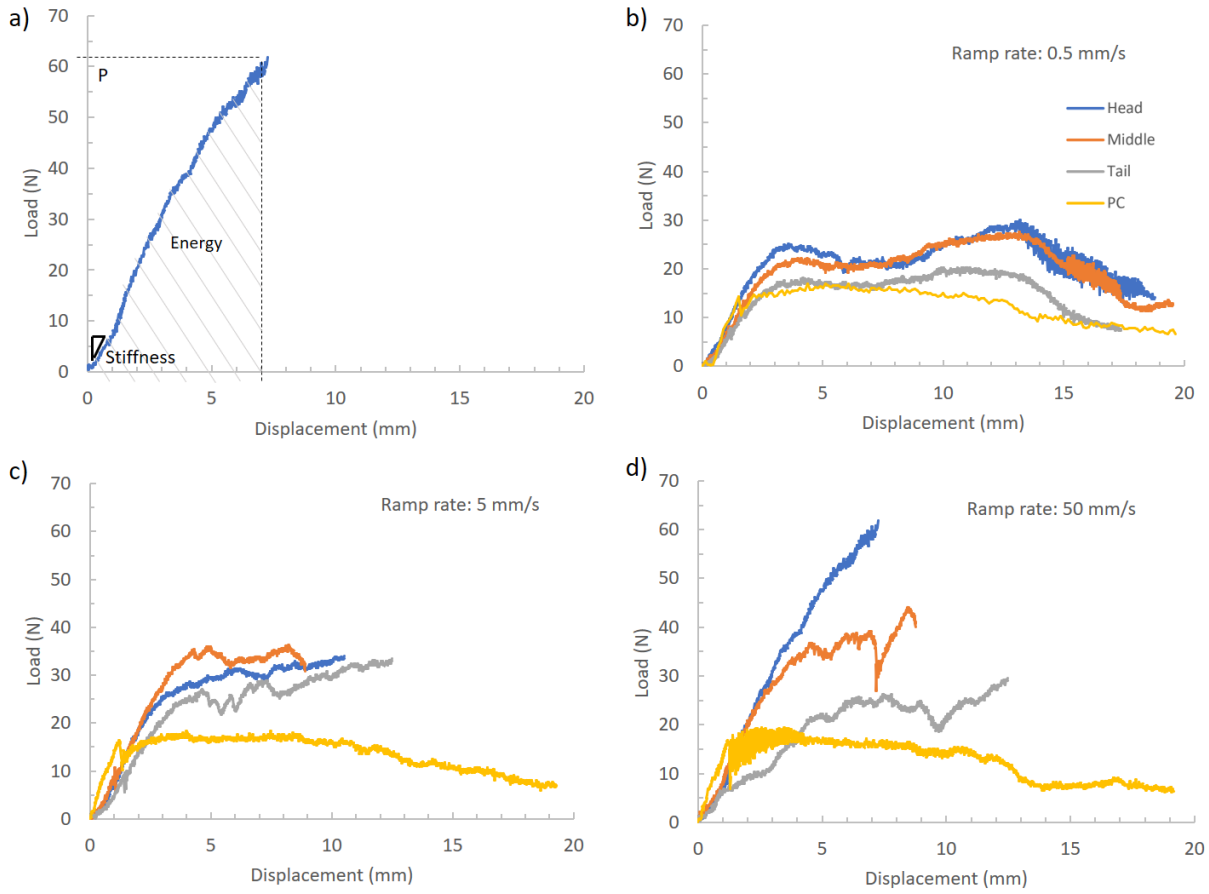

Figure 2.4. Representative puncture responses for the scales from the three regions at three different strain rates. a) response for puncture of a head scale at 50 mm/s. Highlighted are the stiffness, maximum load and work to max load. b) 0.5 mm/s, c) 5 mm/s, and d) 50 mm/s

The influence of loading rate on the puncture resistance of the scales is shown in Figure 2.5. Specifically, individual responses for the stiffness, max load and work to puncture are presented in Fig. 2.5a through 2.5c, respectively, as a function of loading rate. Results for the PC control are also shown for comparison. As evident from the distribution of properties in this figure, there is an increase in resistance to puncture with increasing loading rate for the scales. Similar to the evaluation of the tensile responses, the strain rate sensitivity exponents were estimated for the work to puncture. In the transverse loading arrangement, the values of m for the head, middle and tail were 0.30, 0.25 and 0.39, respectively. For the PC control the exponent was 0.01.

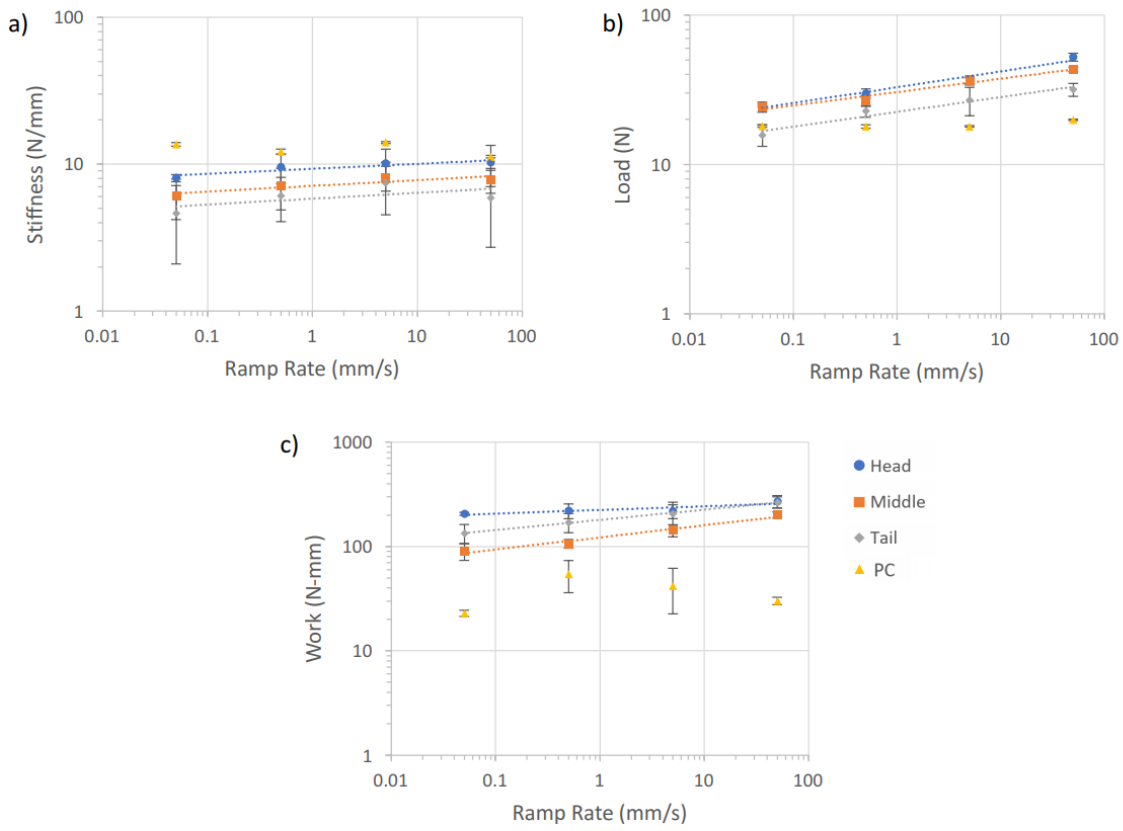

Figure 2.5. Strain rate dependence in the puncture responses of the scales for each of the three regions. (a) stiffness, (b) max load, (c) work to max load.

The transverse puncture responses in Figure 2.5 were plotted without accounting for the geometric differences in the scales, and the scales from the three regions did not have the same thickness. Therefore, the load and work to puncture responses were also evaluated after normalizing by the thickness as shown in Fig. 2.6a and 2.6b, respectively. Interestingly, there is less difference between the responses of scales from the three regions of the fish when plotted in this manner. In fact, the strain rate sensitivity exponent of the normalized load to puncture is not a function of the region, with an average value of roughly 0.15. There is a significant increase in the work to puncture with loading rate when presented in the normalized condition as well, with between 5X to 6X increase over the range in loading rate. In addition, the largest resistance to

puncture is exhibited by the scales of the head region. Clearly the rate sensitivity in the work to puncture is substantially greater than in the energy to failure in uniaxial tension (Fig. 2.4d).

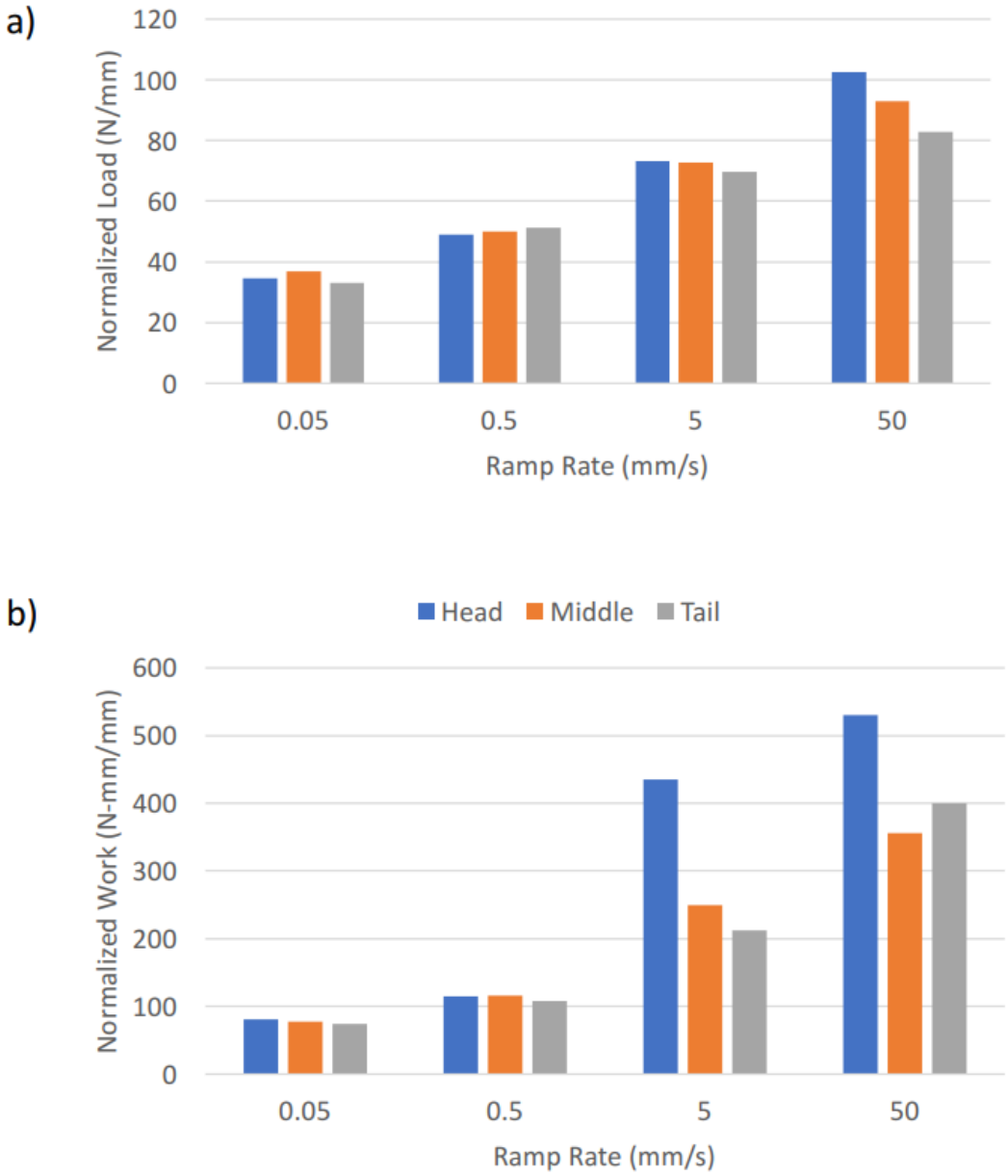

Figure 2.6. Comparison of the relative rate dependence in axial and transverse loading responses of the scales. a) normalized toughness in tension, b) normalized puncture resistance in terms of the work to puncture

MicroCT scanning was performed on the scales after testing to interpret the mechanisms contributing to the difference in structural behavior under the two modes of loading. Selected scans obtained from transverse puncture loading are shown in Figure 2.7. Specifically, scans of the scale cross-section after puncture are shown in Figures 2.7a and 2.7b, and correspond to sections outside of the center of puncture and along the centerline, respectively. Similarly, microCT images of punctured scales shown in-plane to the scale and within the EE and the IE are shown in Figures 2.7c and 2.7d, respectively. According to the cross-section views, the LL and EE layers remain largely intact, without evidence of delamination between the individual plies, or separation between the LL and EE (Fig. 2.7a and Fig. 2.7b). However, a substantial degree of delamination occurred between the individual plies of the IE, as evident in Figure 2.7c. The delamination extends from the axisymmetric center radially and approximately 2X the puncture diameter, as apparent in Figure 2.7c. The delamination occurred throughout the entire IE thickness, not just as a result of splaying within a few of the peripheral plies. In fact, the concert of deformed plies of the Bouligand structure results in clear views of the axial elongation that occurred in fibers of the individual plies (Figure 2.7d).

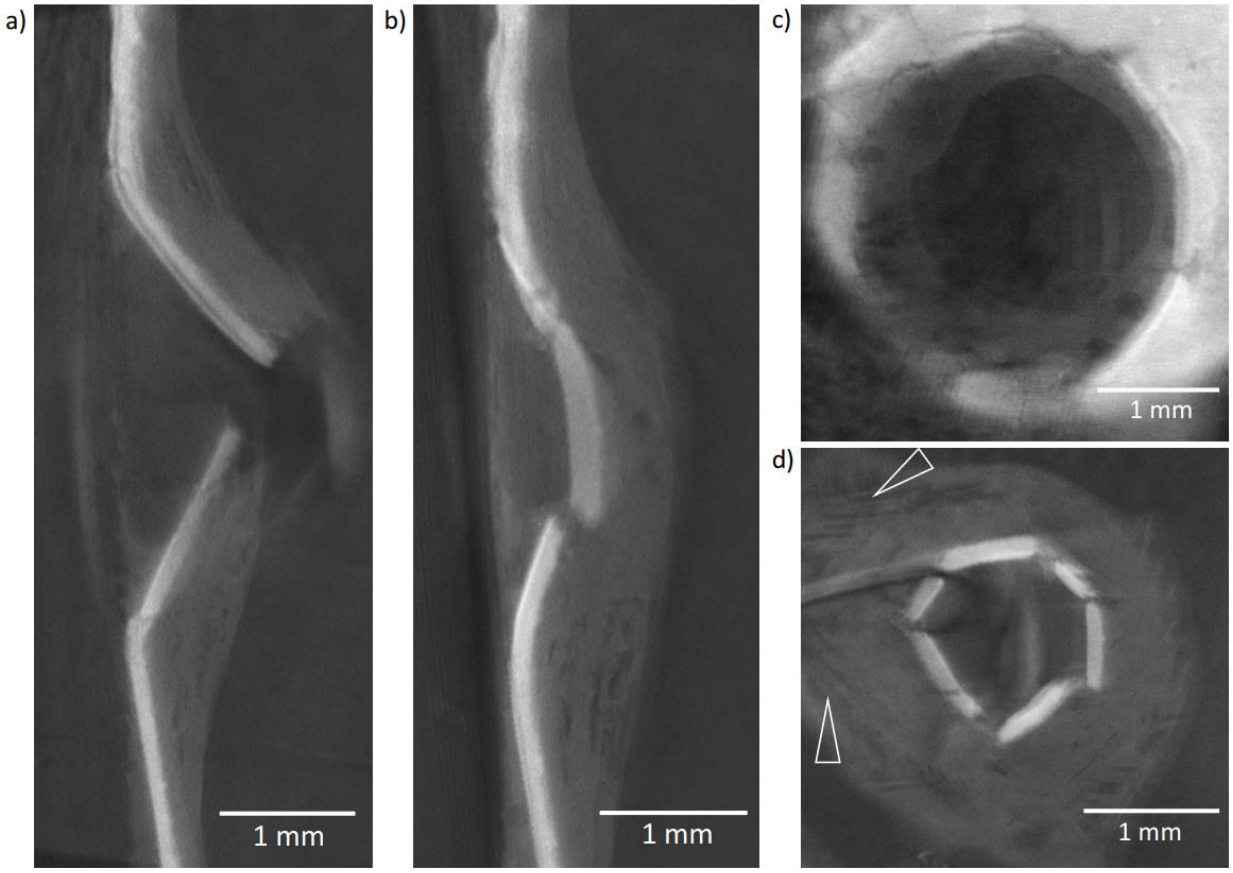

Figure 2.7. MicroCT scans of selected representative scales after transverse puncture loading at 50 mm/s. a), and b) cross-sections at the center of puncture and 1 mm away. c) and d) in-plane views within the LL and within the IE.

2.5 DISCUSSION

Elasmoid fish scales are structural composites that are constructed from an interesting distribution of collagen fibrils and carbonated apatite. These are the same principle building blocks found in most other hard tissues. Mineralized tissues utilize a hierarchical architecture to achieve the desired combination of mechanical properties, but generally exhibit rather limited spatial gradients in mineral content [Currey, 1998]. In contrast, fish scales exhibit structural hierarchy and possesses steep gradients in the degree of mineralization from the limiting layer to the internal elasmodine [Murcia et al., 2016]. The largest mineral gradient occurs over the <100 μm thickness

of the limiting layer, which appears to be key in achieving the competing requirements of flexibility and puncture resistance – or so called “protecto-flexibility” as proposed by Rudykh et al. [2015]. Due to the second mineral gradient of the elasmodine, there is a reduction in hardness and elastic modulus from the LL to the IE of a factor of 10 [Chen et al., 2012; Torres et al., 2014]. This gradient is important to the mitigation of surface stress imposed by puncture and enables dissipation of fracture energy by a combination of elastic and inelastic deformation [Wang et al., 2009]. Furthermore, the sparse mineralization of the elasmodine is responsible for the flexibility and limited resistance to locomotion, but is also considered to be largely responsible for its outstanding toughness and impact resistance [Torres et al., 2015].

The rate dependent structural behavior of fish scales has been previously explored under tensile loading. That effort was focused on the change in elastic modulus with rate [Lin et al., 2011]. A comparison of the increase in elastic modulus with strain rate for the carp scales with arapaima scales and of other tissues after the work of Lin et al., [2014] is presented in Figure 2.8. Included in this figure are results for human femur bone [McElhaney, 1966], bovine cortical bone [Adharapurapu et al., 2006], horn keratin from McKittrick et al., [2010] and rat-tail tendon [Haut and Little, 1972]. The strain rate sensitivity exponent for the elastic modulus of the carp scales in tension ranged from 0.06 to 0.13, with scales from the tail, with lowest overall mineral content, exhibiting the lowest value. These values are substantially less than that reported for the arapaima scales (0.26). It is interesting to note that the carp scales are more compliant than the other tissues, whereas the strain rate sensitivity of the modulus is consistent with that for bone. This similarity could be due to the predominant contribution of the limiting layer to the in-plane stiffness, which exhibits a mineral content that is more comparable to that of bone [Ikoma et al., 2003; Torres et al., 2008].

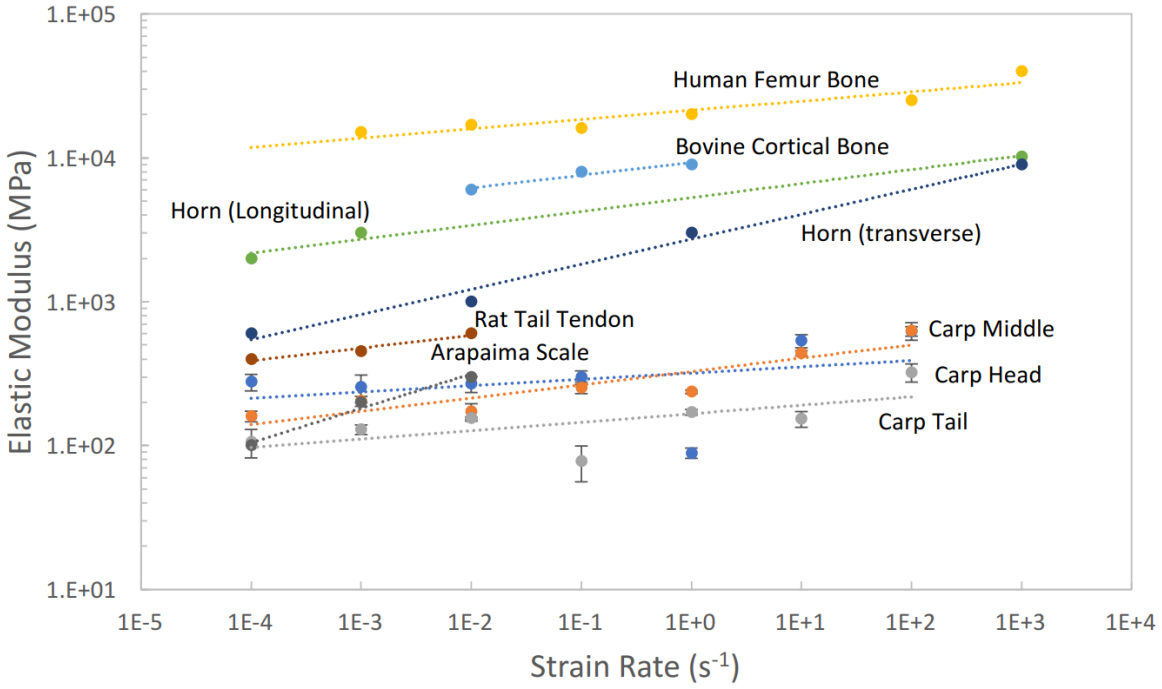

Figure 2.8. A comparison of the strain rate behavior of mineralized tissues with results for the carp scales. Results shown include arapaima scales from Lin et al., [2014], human femur bone [McElhaney, 1966], bovine cortical bone [Adharapurapu et al., 2006], horn keratin from McKittrick et al., [2010] and rat-tail tendon [Haut and Little, 1972].

Results of the experiments showed that there is an increase in the properties defining the resistance to failure with increasing strain rate for both tension (Fig. 2.3) and puncture (Fig. 2.5) loading. However, there are some important differences in the strain rate dependence of the scales between the two different loading formats that warrant attention. For instance, the largest increase in elastic modulus in tension occurs at the highest loading rates, whereas in transverse loading for puncture the stiffness plateaus and then decreases at the highest rate. In addition, both the ultimate strength and strain to failure in tension increase with strain rate until reaching a plateau at 10^1 s^{-1}, after which there is a decrease; that behavior is also reflected in the corresponding toughness of the scales. In contrast, there is an increase in both the max load and the work to puncture over the entire range of loading rates. That response is beneficial for protection from physical threats.

Hence, within the limitations of the range in strain rates used in the experiments, the microstructure of the scales appears to have evolved for superior resistance to puncture loading. The laminated microstructure and mineral gradient promote mechanisms that are effective at resisting puncture and become increasingly potent at higher strain rates.

After accounting for the scale thickness, all three regions exhibited approximately equivalent values of normalized load to puncture (Fig. 2.6a). However, when the corresponding normalized energy to puncture was assessed, the head scales required between 1.5 to 2X greater energy than that achieved by the scales of the middle and tail regions (Fig. 2.6b). Clearly the most vital parts of the fish are located closer to the head, which warrants greater protection in this region. As such, evolutionary processes appear to have introduced spatial variations in the microstructure of scales to achieve enhanced protection in areas of greater need. That comment is admittedly speculative as the results were obtained for only a single species of fish. However, it emphasizes that the spatial variations in scale structure observed within a species could be equally valuable to comparisons across species in pursuing biomimetic design. At the very least, important lessons in bioinspiration may be overlooked without efforts focused on performing site-specific evaluations.

What are the mechanisms responsible for the increase in resistance to failure of the elasmoid scales with loading rate? The strain rate sensitivity is expected to originate primarily from the collagen, its major constituent. Collagen undergoes an increase in resistance to deformation with increasing strain rate [Arumugan, et al., 1992; Shergold et al., 2006; Zhou et al., 2010]. The inter-peptide hydrogen bonds are rate sensitive due to the dependence on water molecules and their dispersion during deformation. However, the rate sensitivity reported for collagen is much lower than exhibited by the scales. The next contribution occurs at the ply level. Zimmermann et al. [2013] commented that the Bouligand-type structure of scales allows the lamina to reorient

according to the loading orientation during in-plane tension. Some of the off-axis laminae undergo a reorientation to the tensile axis and then deform in tension through stretching/sliding mechanisms. The laminae with larger angles of misalignment sympathetically rotate away from the tensile axis. Similar observations were noted by Yang et al [2014] in their evaluations of the tensile responses of arapaima scales. This combination of mechanisms enhances the resistance to fracture and toughness of the scales under in-plane tension.

The differences in strain rate sensitivity suggest that the participating mechanisms in transverse loading and localized puncture are less effective than those in tension. In tension, toughening occurs primarily through the inelastic deformation of the collagen, as well as by further deformation enabled by in-plane ply rotations of the off-axis plies. Although the latter mechanism did not contribute substantially in the puncture responses as evident in Fig. 2.7, the rate sensitivity in the work to puncture was substantially greater. This is where visualization of the punctured zone by microCT scanning is most rewarding. The cross-section images of the puncture sites show that the EE undergoes fracture in a brittle manner away from the center of puncture, rather than simply at the apex (Fig. 2.7a). That process distributes the puncture load over a broader area, which incubates delamination between the plies and an extension of damage farther from the immediate puncture zone. The individual plies of the internal elasmodine do not experience failure, but they all undergo a substantial extent of inelastic deformation in tension. By virtue of the out-plane bending, each ply primarily undergoes uniaxial tension, and the assembly of plies work as a cohesive net to further restrain the penetration as evident in Figure 2.7d; this is consistent with the interpretation of Zhu et al., 2013. In addition, the plies are subject to substantial shear coupling at their interfaces due to their differences in orientation, which leads to delamination. Collectively, these processes promote extensive consumption of energy via new surface generation and through

more effective recruitment of contributions at the ply level than in tension. While in-plane tension is essential for characterizing the constitutive behavior of the scales, it does not involve the same mechanisms as those enrolled during protection from puncture threats. Hence, within the limitations of the experimental evaluations performed, it appears that the microstructure of elasmoid scales has evolved to achieve optimal "protecto-flexibility" in favor of its performance corresponding to resistance to in-plane loading.

The results of this investigation contribute new fundamental understanding on the importance of the elasmoid scale microstructure to the tensile and puncture loading responses. Despite the value of the findings, there are some concerns and limitations to the investigation that are important to address. For instance, the experiments were focused on the properties of individual scales, rather than multiple scales acting as a unit. Elasmoid scales are arranged in a pattern with overlapping arrangement. Previous work involving quasi-static loading [Khayer et al., 2013] showed that the stacking arrangement of scales amplifies the overall puncture resistance. While that study did not find contributions from the compliant substrate backing to the puncture resistance of the scales, it was important to the type of damage that may be incurred to the fish (contusion rather than puncture). The use of a backing was considered in the present study, but proved to be a complicating factor when results from the tension and puncture loading formats are compared. Nevertheless, the dynamic response of the scales in the stacked arrangement and on top of a compliant foundation may be important to the apparent strain rate dependence in properties, and should be considered in future work.

An additional concern is that the experiments were limited to carp scales. The focus of this investigation was the spatial variations in dynamic response of the scales from a single species of fish with elasomoid scales. Despite the consistency in elastic modulus of the carp scales with those

of the arapaima in Lin et al [2011], the latter shows a greater increase in stiffness with strain rate (Fig. 2.8) than for the carp. That could be a function of the thicker limiting layer [Murcia et al., 2017b], differences in the number of plies and their stacking sequence [Murcia et al., 2017a] or perhaps the greater extent of the external elasmodine of the total scale thickness. Of note, the work of Lin et al [2011] involved three strain rates to define the response of the arapaima, and at the lowest rates of the range explored here. As evident from Figure 2.4, the rate sensitivity was not constant over the entire range of strain rates evaluated, which could be a relevant contribution to the difference between the arapaima and carp. Despite these concerns, the results provide a greater understanding of the contributions from the microstructure of fish scales to their dynamic loading response. Considering the large diversity of fish species and the unique structure of their scales [Sherman et al., 2016; Murcia et al., 2017], there is much more opportunity to explore and learn from this material system.

2.6 CONCLUSIONS

An experimental investigation of the dynamic loading responses of elasmoid fish scales was conducted including in-plane axial tension and transverse puncture. Samples were obtained from the scales of three different regions (head, middle and tail) of carp fish, and evaluated in the fully hydrated condition at strain rates ranging from 10^{-4} to 10^{2} s^{-1}. There was a significant increase in the resistance to failure with strain rate for both loading orientations. However, when evaluated in terms of the strain rate sensitivity exponent, the values for transverse loading (0.35) were over three times greater than that than for in-plane tension (0.10). The work to puncture of scales increased by roughly 6X over the four-decade increase in the strain rate. The puncture resistance was greatest in scales from the head region overall, which appears to be attributed to

the larger thickness of the mineralized layers in those scales, in comparison to the other regions. Based on the results, spatial variations in the puncture resistance and the so-called “protecto-flexibility” quality of scales are achieved by modulating the external elasmodine and the extent of the limiting layer. The orientation of the interfaces between the lamina and the delamination that occurs between them during puncture loading appear to be the key contributions to the strain rate sensitivity and increased protection during the dynamic loading of physical threats.

Chapter 3. EFFECT OF POLAR ENVIRONMENT ON CYPRINUS CARPIO IN UNIAXIAL AND TRANSVERSE LOADING

3.1 SYNOPSIS

The scales of fish are a natural dermal armor. They are laminated composites that consist of plies of unidirectional collagen fibrils with twisted-plywood stacking arrangement. Based on their composition, the toughness of scales is dependent on the intermolecular bonding within and between the collagen fibrils, and could be potentially improved by increasing the extent of this bonding. In this investigation, the dynamic loading response of fish scales was evaluated in uniaxial tension and transverse puncture, and within liquid environments of water, or a polar solvent (i.e. ethanol) to increase intermolecular bonding. The apparent toughness of the scales increased with loading rate in both tension and puncture. The largest resistance to puncture overall was achieved by scales of the head region after exposure to ethanol, but the largest increase in resistance to failure occurred to scales of the tail (a factor of nearly 7X) due to the larger propensity for interpeptide bonding. Overall, the results showed that the impact resistance of bioinspired composite materials should enroll constituents and complimentary processing that capitalize on interfibril bonds.

3.2 INTRODUCTION

Fish scales are an interesting structural material that serve an important role as flexible armor [Ikoma et al., 2003; Bruet et al., 2008; Torres et al., 2008; Song et al., 2011; Meyers et al., 2012; Yang et al., 2013b; Yang et al., 2014]. Consistent with other forms of dermal armor [e.g. Chen et al., 2011; Yang et al., 2013a; Sun and Chen, 2013; Chen et al., 2014; Chen et al., 2015; Wang et

al., 2016; Achrai and Wagner, 2017], fish scales have been identified as a source of inspiration in the design and development of bioinspired materials for protection [Browning et al., 2013; Zhu et al., 2013; Chintapalli et al., 2014a; Rudyk et al., 2015; Martini and Barthelat, 2016].

The scales of modern fish have evolved into four primary groups including cosmoid, elasmoid, ganoid and placoid scales [Sire and Huysseune, 2003; Kardong, 2006]. The primary building blocks of the scales in each of these groups are apatite and type I collagen fibers [Lin et al., 2011; Garrano et al., 2012; Zhu et al., 2012; Gil-Duran et al., 2016]. In contrast to the flexibility of elasmoid scales, the other three are relatively stiff due to their larger thickness and the presence of bony regions that possess higher mineral content [Sherman et al., 2017]. The flexibility of these scale assemblies is achieved by articulation between the scales, rather than flexure of the scales themselves. Elasmoid scales are much thinner and stacked or over-layered with respect to one another. They are more commonly found on fish with greater speed, and are clearly multi-functional in light of their required flexibility and puncture resistance [Bruet et al., 2008; Jandt, 2008]. Indeed, elasmoid scales are inspiring the designs of protective "skins" with imbricated scale-like structures [Rudyk et al., 2015].

The microstructure of elasmoid scales consists of two primary layers, including a thin outermost highly mineralized layer, and the secondary interior layer, which occupies the bulk of the scale thickness (Figure 2.1a). The outermost Limiting Layer (LL), is a highly-mineralized matrix of calcium-deficient apatite crystals that is reinforced by a sparse dispersion of collagen fibers [Zylberberg 1982]. The underlying elasmodine is a laminate of sparsely mineralized unidirectional type I collagen fibril plies. The elasmodine actually consists of two separate layers [Murcia, et al., 2015], both consisting of discrete plies of unidirectional collagen fibers with specific stacking sequence [Murcia et al., 2017]. The internal elasmodine (IE) and the external

elasmodine (EE) are only differentiated by the higher mineral content of the latter [Garrano et al., 2012]. Yet, they both have substantially lower mineral content than the LL [Murcia et al., 2016]. The plies of the entire elasmodine are arranged in the form of a twisted-plywood structure, with rotation between plies ranging between 60–90° depending on the fish [Bigi, 2002]. For the carp, the average angle of rotation between plies is 75°, in comparison to close to 90° rotation for the arapaima [Murcia et al., 2017].

The development of bioinspired structural materials generally involves mimicking the morphology of existing natural systems with an appropriate set of synthetic material analogues and methods of processing [Wegst et al., 2015]. Nevertheless, biological structural materials can also serve as a vehicle for exploring new approaches to amplify strength and toughness of synthetic materials [Meyers et al., 2011; Barthelat and Mirkhalaf, 2013], or to explore ways to activate property changes in response to a stimulus. For instance, in a recent study by [Murcia et al., 2016] the stiffness and strength of elasmoid scales were increased by exposure to a polar solvent. The change in mechanical behavior was nearly instantaneous and caused by interpeptide hydrogen-bonding of the collagen that resulted from the displacement of water molecules by ethanol (a weaker hydrogen-bond-forming solvent). The removal of water allows hydrogen-bonds to develop between the peptide chains [Pashley et al., 2003]. Although hydrogen bonds are rather weak due to their lower energy in comparison to the covalent bonds, an adequately high number of interpeptide bonds can initiate substantial changes to the mechanical behavior of single fibrils [Grant et al., 2009], and dense fibril systems [Maciel et al., 1996; Nyman et al., 2008].

In contrast to the increases in tensile strength and stiffness of fish scales with exposure to ethanol, Murcia et al [2016] reported that the change in the Mode III tear resistance to failure was minimal. The different behaviors in tension and out-of-plane shear was interpreted to result from

the interference of interfibril bonding and mineral to the reorientation of the collagen fibrils in Mode III tear failures. However, Nalla et al [2005, 2006] showed that exposing tooth dentin to polar solvents, a relatively highly mineralized tissue, caused a significant increase in its resistance to crack growth under Mode I loading. Thus, the nature of loading and relative mineral content appear to be important to the effects of interfibril bonding.

The design of fish scales has evolved to be resistant to puncture, which occurs through dynamic loading. While the resistance to indentation and puncture of scales has received considerable attention [e.g. Wang et al., 2009; Chen et al., 2012; Meyers et al., 2012; Allison et al., 2013; Zhu et al., 2013; Torres et al., 2014; Khayer Dastjerdi and Barthelat, 2015], the importance of dynamic loading has not [Lin et al., 2011]. In addition, the effect of interpeptide bonding to the strain-rate characteristics of fish scales has not been reported. Therefore, in this investigation the mechanical behavior of elasmoid fish scales was evaluated under uniaxial tension and transverse puncture over a large range of strain rates. The primary objectives were to evaluate the effect of interpeptide bonding on the toughness of the scales in each loading orientation and to assess the its relative importance as a function of loading rate. The roles of mineral reinforcement and interpeptide bonding on the resistance to failure of the scales is examined and the importance of the findings to bioinspired designs of protective materials is discussed.

3.3 Materials and Methods

Scales of the *Cyprinus carpio* (i.e. the common freshwater carp) were obtained by extraction from across the body of several fish. These fish were marketed as East Asian carp, and no additional information was available. The scales were obtained nearly equidistant between the ventral and dorsal aspects of the body (i.e. adjacent to the midline) and from three regions including

near the head, mid-length (beneath the dorsal fin) and near the tail. To be consistent in collection for all fish, these regions were defined at distances from the gill plate of approximately 15%, 40% and 80% of the total number of scales counted along the lateral line over the fish length. All of the scales were less than 1 mm thick and possessed a diameter that varied according to the anatomical position.

After extraction, the scales were either stored in Hanks Balanced Salt Solution (HBSS) at room temperature or in an ethanol bath at room temperature for minimum of 24 hours. The effectiveness of polar solvents to form hydrogen bonds in collagen is often described in terms of the Hansen solubility parameter for hydrogen bonding (δ_h). Polar solvents with high δ_h values preferentially form hydrogen bonds with collagen peptides, thereby preventing the molecules from developing interpeptide bonds. Water has one of the highest reported δ_h values for polar solvents 37.3 $(J/cm^3)^{1/2}$. In the absence of water, or when the matrix is immersed in solvents with δ_h below 19 $(J/cm^3)^{1/2}$, which is the value postulated for collagen in air [Pashley et al., 2003], interpeptide hydrogen bonding occurs. Thus, exposure of the scales to ethanol with δ_h of 19 $(J/cm^3)^{1/2}$) is expected to cause an increase in the stiffness and strength of the scales due to the displacement of water molecules and development of interpeptide hydrogen bonds [Ramachandran, Chandrasekharan, 1968].

To support an evaluation of the tensile properties, conventional dog-bone shaped tensile specimens were sectioned from the scales using a punch and stamping process [Garanno et al., 2012]. A single specimen was stamped from the center region of each scale where the thickness is most uniform. The specimens possessed a gage section length and width of 5.5 mm and 1.5 mm, respectively (Figure 2.1b). All of the specimens were obtained with alignment parallel to the fish length, for consistency, as scales from the head region can exhibit anisotropic behavior

[Murcia et al., 2015]. After sectioning, the specimens were placed in a bath of HBSS or ethanol at room temperature.

Tensile testing of the hydrated fish scale specimens was performed to failure at room temperature. The loading was performed under displacement control using a commercial universal testing machine (Instron ElectroPuls E1000, Norwood, MA, USA) equipped with load cell having full-scale range of 250 N and load precision of 0.01%. Stroke rates were selected to obtain strain rates from $1x10^{-4}$ to $1x10^{2}$ s^{-1} in decades, which were estimated according to the specimen gage length. All specimens were tested to failure. Five specimens were evaluated for each strain rate and anatomical region (head, middle and tail), which resulted in 7 rates x 3 regions x 5 specimens = 105 total tests for each liquid environment. Results of the experiments performed on the scales tested in HBSS were also reported in Ghods et al. [2017] to explore the strain rate dependence of the mechanical behavior. An additional 105 experiments were performed on the scales subjected to the ethanol treatment.

The elastic modulus (E), strength (S) and modulus of toughness (MOT) were determined from results of the tension tests at each rate using the engineering stress-strain definitions. The elastic modulus was determined using the tangent method for strains less than 1% and the strength was defined by the maximum stress realized by the sample. The modulus of toughness was calculated by integrating the area under the stress-strain curves as a function of strain until failure.

Puncture tests were conducted on specimens from the three anatomical regions using a sharp stainless steel punch with tip radius of curvature = 40 um and included angle of ≈ 30°). Loading was conducted using a universal testing machine (Model ELF 3300, BOSE, Eden Prairie, MN, USA) on scales clamped within a dedicated fixture at rates that ranged from $5x10^{-2}$ to 50 mm/s.

The scales were unsupported and clamped around the periphery with exposed portion of 12.5 mm as shown in Figure 2.1c. With an average thickness of approximately 0.5 mm, and ignoring the out of plane deflection, the loading rates corresponded to effective strain rates of approximately $1x10^{-1}$ to $1x10^{3}$ s^{-1}; the actual strain rates for the puncture tests varied according to the scale thickness. In all testing the scales were arranged with limiting layer oriented towards the punch. The load and displacement signals were acquired at a rate of 4 kHz. Similar to the evaluation performed using tensile loading, five specimens were evaluated for each strain rate and anatomical region (head, middle and tail), which resulted in 4 rates x 3 regions x 5 specimens = 60 tests for each liquid environment. Results of the experiments performed with HBSS storage were reported in Ghods et al. [2017] to evaluate the strain rate dependence of the impact behavior. An additional 60 puncture experiments were performed on the scales subjected to the ethanol treatment, for a total of 120 experiments overall.

The scale performance under puncture loading was evaluated in terms of the stiffness at the onse of loading, the load to initiate and complete puncture, as well as the corresponding work to puncture. The measures of work were obtained by integrating the load load-line displacements to the displacement of interest.

The microstructure of scales within each region of evaluation was examined using scanning electron microscopy (JEOL, Model JSM- 6010PLUS/LA, Peabody, MA). The samples were sputtered with Au/Pd and observed in secondary electron imaging mode. In addition, selected scales were evaluated after puncture testing using microCT scanning with a North Star Imaging X5000. For this effort, the scales were treated with a very light coating of diluted ethylene glycol after Ryou et al., [2013] to maintain the moisture content within the scale and to minimize any distortion related to dehydration during scanning. Scales from the head region were scanned after

completion of testing at a loading rate of 50 mm/s. The scans were performed using 50 kV and 1000 uA, 1 frame/sec step scan mode with 10 ms delay, 900 projections, and two frame averaging. These conditions were identified as most appropriate for evaluating the scales via preliminary studies. Based on the fixture arrangement of the scales, x-ray source and detector characteristics, a geometric zoom of approximately 50X was achieved and with a resolution of 3 um/pixel. Radiographs were treated using the systems imaging software (efX-CT, Version 1.6, North Star Imaging, Rogers, MN, USA) to obtain images of relevance for display.

3.4 RESULTS

Typical stress-strain responses resulting from the uniaxial tension tests are shown in Figure 3.1. A single response obtained for a scale from the middle region evaluated after ethanol treatment and at a rate of $1x10^{1}$ s^{-1} is shown in Figure 3.1a. The definitions of the elastic modulus (E), strength (S) and modulus of toughness (MOT) are shown, which were used as metrics to quantitatively characterize the tensile responses of the scale samples. Representative responses obtained at low (10^{-3} s^{-1}), intermediate (10^{-1} s^{-1}) and high (10^{1} s^{-1}) strain rates are in shown in Fig. 3.1b through 3.1d, respectively. These graphs include an example from scales at each of three regions and under both water and ethanol treatment conditions. A comparison of the responses in these figures shows that there is an increase in the resistance to fracture increases with ethanol treatment and with increasing loading rate.

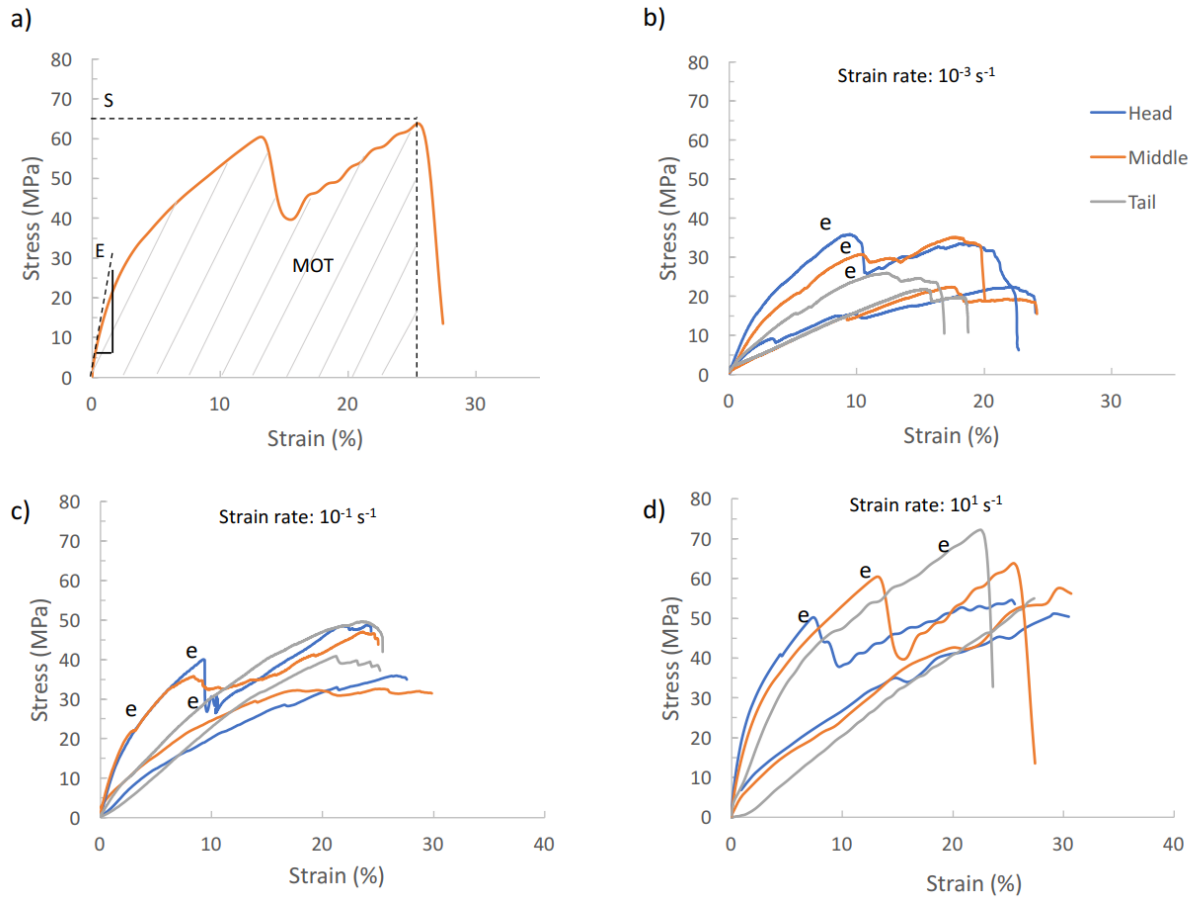

Figure 3.1. Representative stress-strain responses for scales from the three representative regions at three different strain rates. a) response for a scale from the middle region tested in ethanol with definition of the measured properties. E, S and MOT represent the elastic modulus, strength and modulus of toughness, respectively. b) 10^{-3} s^{-1}, c) 10^{-1} s^{-1}, and d) 10^{1} s^{-1}. Those responses marked with e = ethanol treatment.

The contribution of loading rate to the elastic modulus, strength, strain to failure and modulus of toughness of the scales is shown in Fig. 3.2a through 3.2d, respectively. The results in each graph represent the average response of scales from the three regions, namely the head, middle and tail, as well as within both water and ethanol environments. In general, there is an increase in all four mechanical properties of the scales with loading rate, and in both aqueous

environments. In water, the elastic modulus underwent the largest increase in magnitude with strain rate (up to 3X); the smallest increase with loading rate was found in the strain to fracture (less than 1.5X), as shown in Fig. 3.2c. Similarly, after ethanol treatment, the elastic modulus underwent the large increase with strain rate (by nearly 6X) and the strain to fracture was least affected by the ethanol condition. Both the tensile strength and modulus of toughness of the scales subjected to ethanol increased by approximately 3X over the range of strain rate.

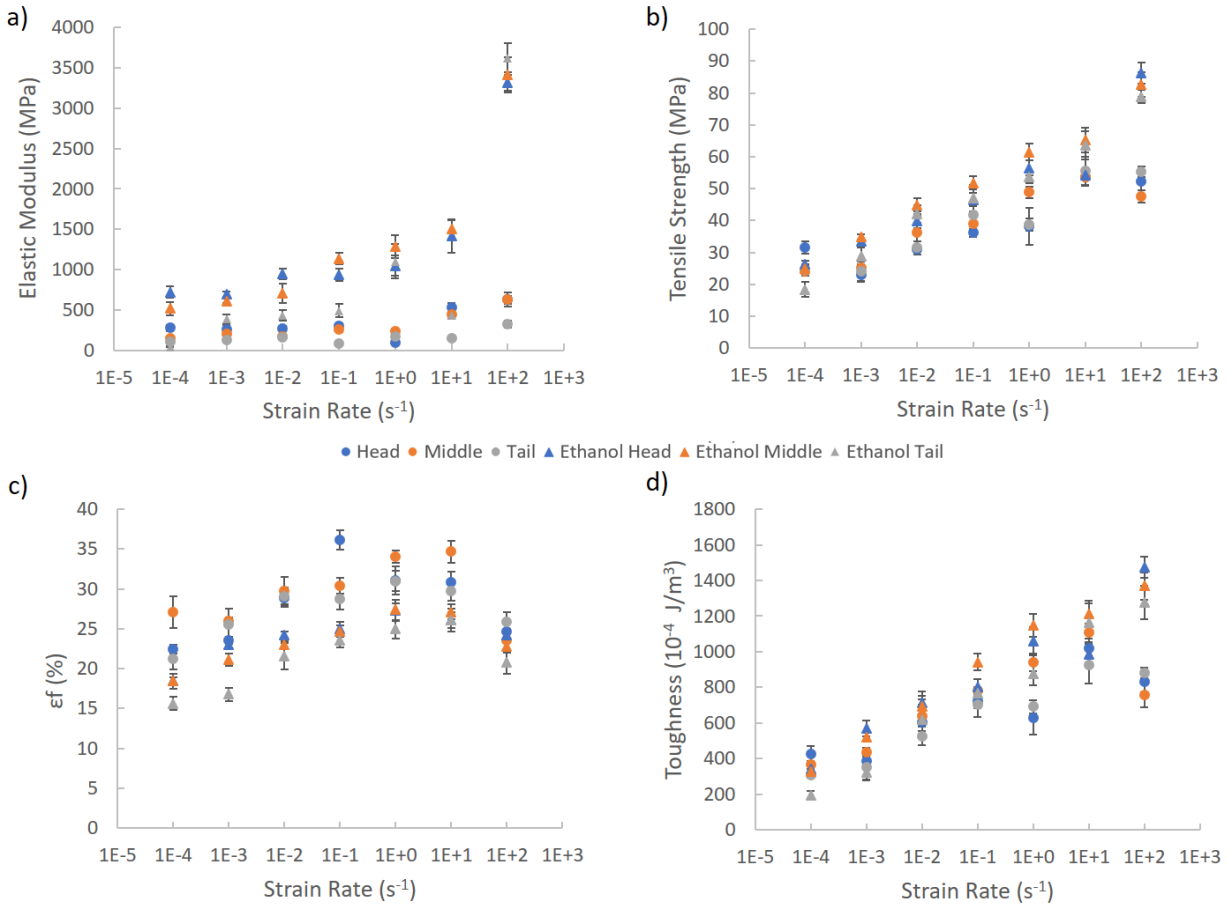

Figure 3.2. Strain rate dependence in the tensile responses of the scales for each of the three regions. (a) elastic modulus, (b) ultimate tensile strength, (c) strain to failure (ε_f), and (d) modulus of toughness.

The strain rate sensitivity of the scales was estimated from the measures of toughness for each of the three regions. A power law response was adopted to characterize the responses, in which the toughness (T) was defined according to $T = B\dot{e}^m$ where m and B represents the strain rate sensitivity exponent and coefficient, respectively. In tension, the values of m for the head, middle and tail regions evaluated in water were approximately 0.06, 0.07 and 0.08, respectively. After ethanol treatment, the values of m for the head, middle and tail regions were 0.09, 0.10 and 0.13, respectively. Exposure to ethanol resulted in between 30% and 50% increase in the strain rate sensitivity, with the largest occurring in scales from the tail region.

A representative load vs load-line displacement response for transverse puncture loading of a scale to failure is shown in Fig. 3.3a. This response was obtained for a scale from the middle region evaluated after ethanol treatment and at a loading rate of 5 mm/s. There are three events highlighted in this figure, including: i) where the punch initiates puncture and penetrates the LL at elasmodine, ii) where the maximum load occurs during the puncture process, and iii) in which the punch completely penetrates the scale beyond its tapered neck. The failure process is characterized by the apparent stiffness at the onset of loading, the load and work to initiate puncture defined at point (i), the maximum load to failure (P_{max}) defined at point (ii) and the work to failure defined at point (iii). These quantities were used for comparing the mechanical behavior of the scale samples. Representative puncture responses for selected low (0.5 mm/s), medium (5 mm/s) and high (50 mm/s) loading rates are shown in Fig. 3.3b through 3.3c. The graphs include typical responses for the three regions of evaluation and within both the water and ethanol environments; those evaluated in ethanol are marked accordingly (e). In general, the resistance to failure increased with increasing loading rate in both aqueous environments. However, in contrast to the increase in apparent inelastic strain to failure of the scales with loading rate in tension, the puncture

displacement to failure did not increase with loading rate as evident from comparing the responses from Fig. 3.3b to 3.3d.

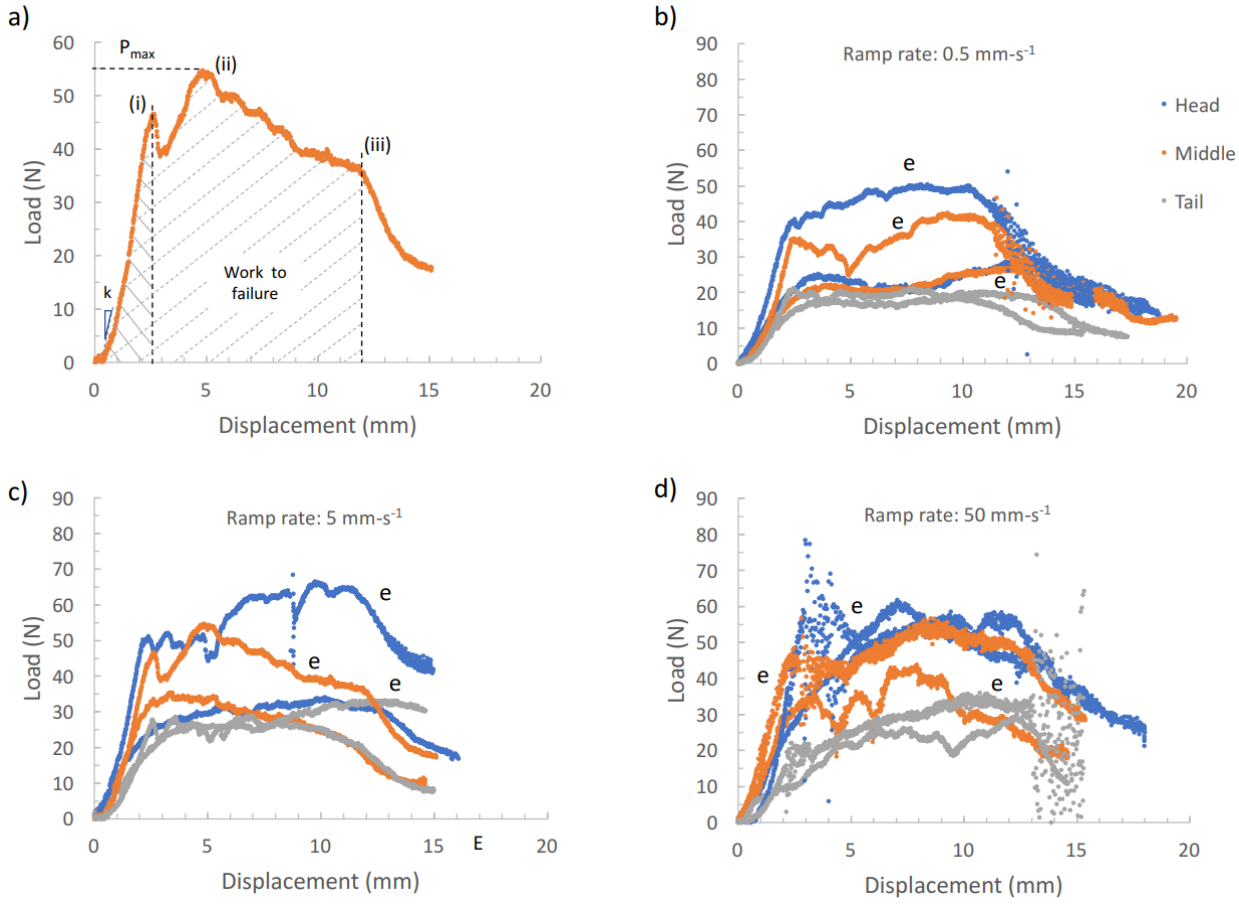

Figure 3.3. Representative puncture responses for the scales from the three regions at three different strain rates. a) response for puncture of a middle scale at 5 mm/s. Highlighted are the stiffness (k), load and work to puncture (defined at i), max load to failure (defined at ii), and work to failure (defined at point iii). b) 0.5 mm/s, c) 5 mm/s, and d) 50 mm/s. Those responses marked with e = ethanol treatment.

The influence of loading rate on the puncture resistance of the scales and importance of ethanol treatment is shown in Figure 3.4. Specifically, the cumulative responses for the stiffness, as well as the load and work to failure are presented in Fig. 3.4a through 3.4c, respectively, over

the range in loading rate evaluated. As evident from the trends in data, there is an increase in each of the properties with increasing loading rate, and for both the water and ethanol treatment conditions. Note that results for the puncture displacement to failure are not shown as there was no distinct trends in the data. Akin to evaluating the tensile responses, the strain rate sensitivity exponents (m) were estimated for the work to failure. In the hydrated condition the values of m for the head, middle and tail were 0.13, 0.11 and 0.11, respectively. After ethanol treatment, the values of m for the head, middle and tail regions were 0.06, 0.04 and 0.06, respectively. Exposure to ethanol increased the resistance to puncture, but resulted in between 40% and 70% decrease in the strain rate sensitivity.

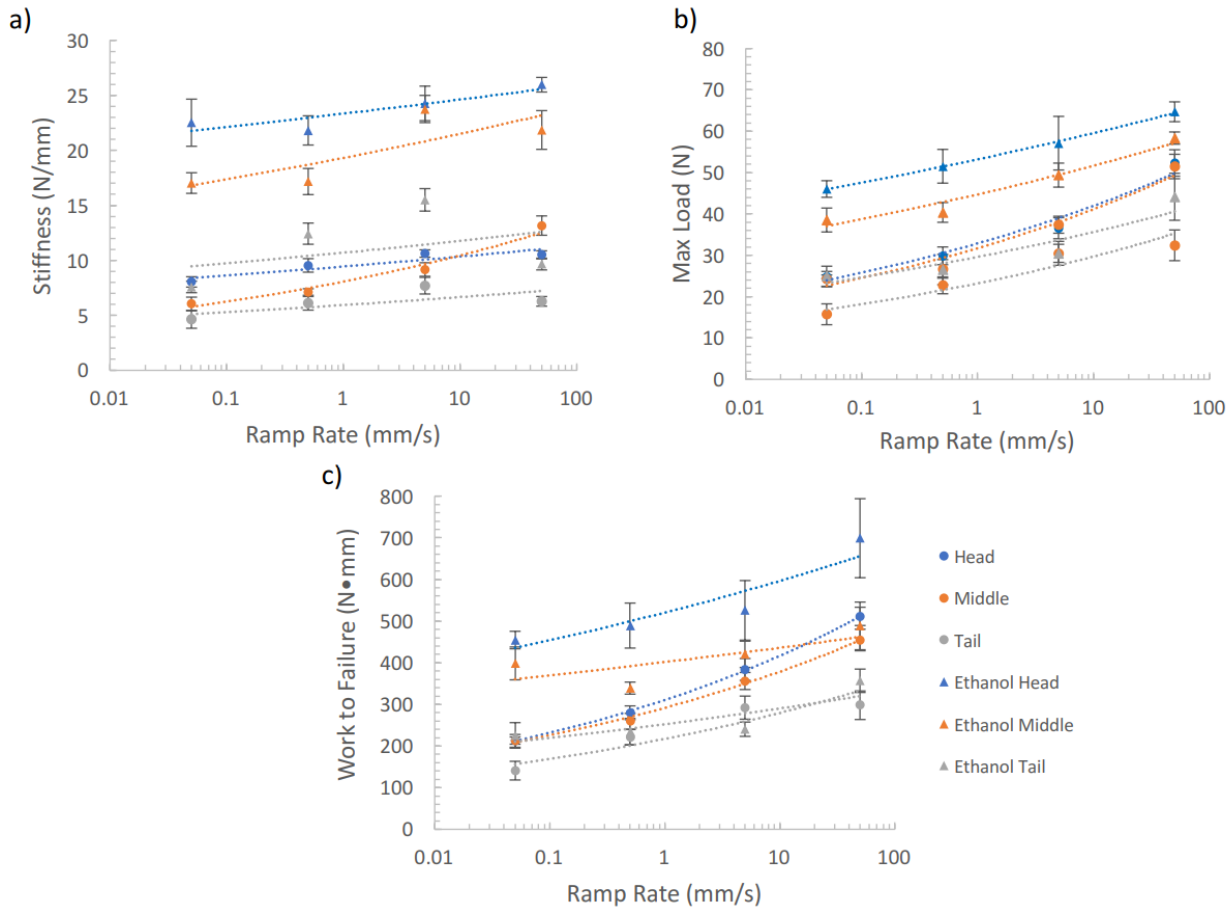

Figure 3.4. Strain rate dependence in the puncture responses of the scales for each of the three regions. (a) stiffness, (b) max load to failure, (c) work to failure.

To further explore the importance of loading rate and ethanol treatment on the resistance to puncture of the scales, the properties obtained at the lowest loading rate (0.05 mm/s) were used to normalize the responses obtained at the higher rates and after ethanol testing. The results of this analysis are shown in Figure 3.5. Specifically, the load and work to the initiation of puncture, i.e. defined as the initiation of penetration of the punch (pt (i) in Fig. 3.3a, are shown in Figure 3.5a and 3.5b, respectively. According to the normalization scheme, the results for the head, middle and tail obtained for loading at 0.05 mm/s in water are unity. The properties at the higher loading rates and after ethanol treatment are >1, indicating that those conditions caused an increase. According to Figure 3.5a, the scales underwent an increase in the resistance to puncture with loading rate, and although ethanol exposure was important at the lowest rate, it was not important to the load to initiate puncture at the higher rates of loading. There was also an increase in the work required to initiate puncture with loading rate (Fig. 3.5b). However, ethanol exposure caused the largest increase in work to puncture, with up to 7X greater required work to puncture than that required when hydrated. The normalized load and work to failure, i.e. defined as the complete penetration of the punch, are shown in Figure 3.5c and 3.5d, respectively. In general, there is an increase in both the load and work required to failure with loading rate for the three anatomic regions of the scales. The largest increase in these properties occurred as a result of ethanol exposure. In the load to puncture, all three regions exhibited similar increases as a result of the ethanol. That is not consistent with the work to puncture, which increased the most in the scales of the tail region.

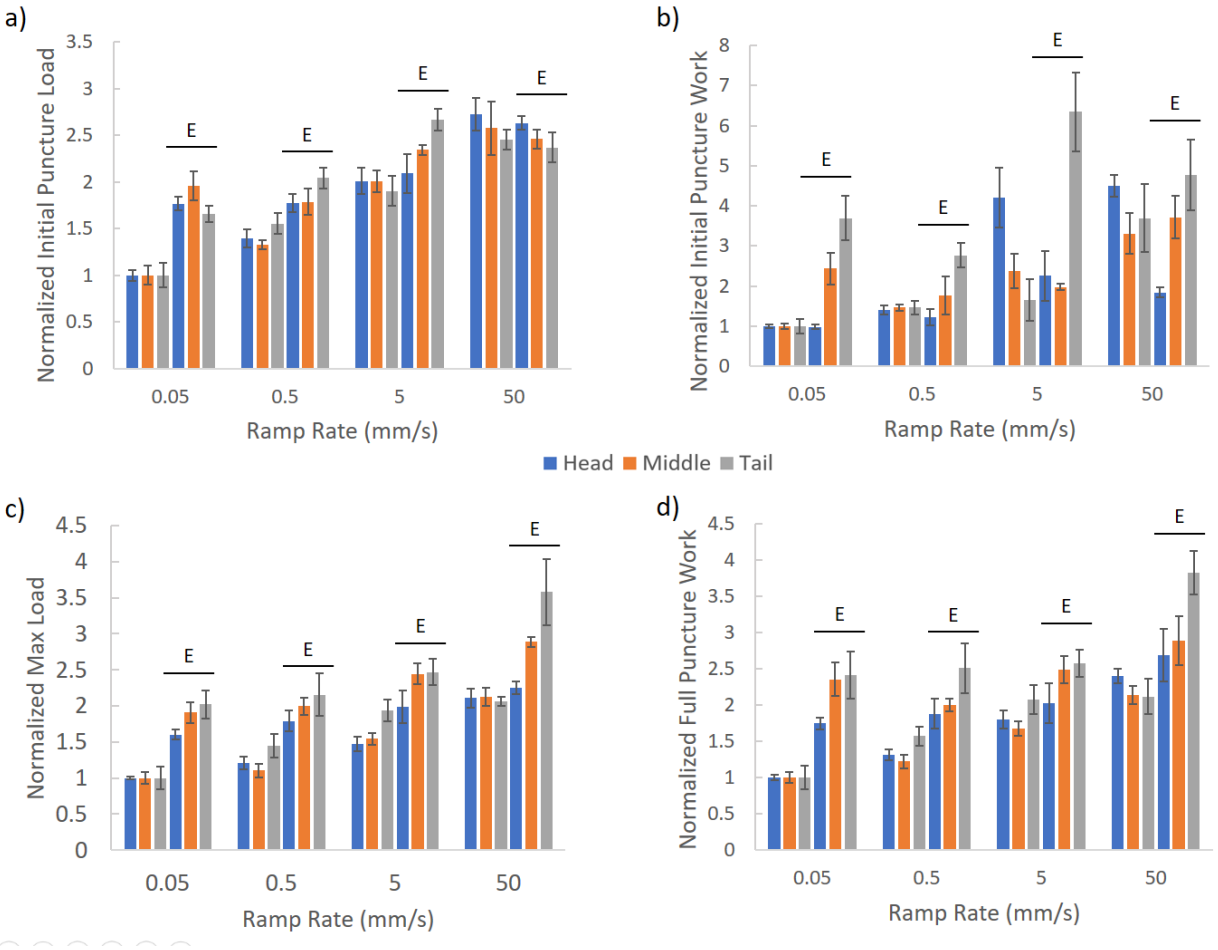

Figure 3.5. Comparison of the rate dependence in the normalized puncture responses. a) normalized load to puncture, b) normalized work to puncture, c) normalized max load to failure, and d) normalized work to failure.

After completion of the puncture testing, representative scales were evaluated by microCT scanning to investigate contributions to the structural behavior in the water and ethanol conditions. Representative microCT scans obtained from transverse puncture loading are shown in Figure 3.6. Scans of scales punctured at 50 mm/s in water and ethanol are shown in Figures 3.6a and 3.6b, respectively. These are cross-section views at the centerline of the puncture. Similarly, microCT images representing "in-plane" views of punctured scales evaluated in water and ethanol are shown

in Figures 3.6c and 3.6d, respectively; the depth of this cross-sectional slice is within the IE region of the scales. Note that the bright regions within these figures are the combined LL and EE, which exemplify their higher mineral content relative to the IE. The cross-section views show that the LL and EE layers remain largely intact, without delamination or separation between the LL and EE (Fig. 3.6a and Fig. 3.6b). There is evidence of delamination between individual plies of the IE, particularly for the hydrated scale in Figure 3.6a. In Figure 3.6c, the delamination extends radially outward and approximately 2X the puncture diameter. In contrast, the disruption in plies of the ethanol treated scales is much different than the hydrated scales; the delamination appears to have occurred profusely throughout the entire IE thickness (Fig. 3.6b), and not confined to within specific interfaces. In addition, the extent of delamination from the center of puncture outwards is much less in the ethanol treated scale (Fig. 3.6d) than in the hydrated scale.

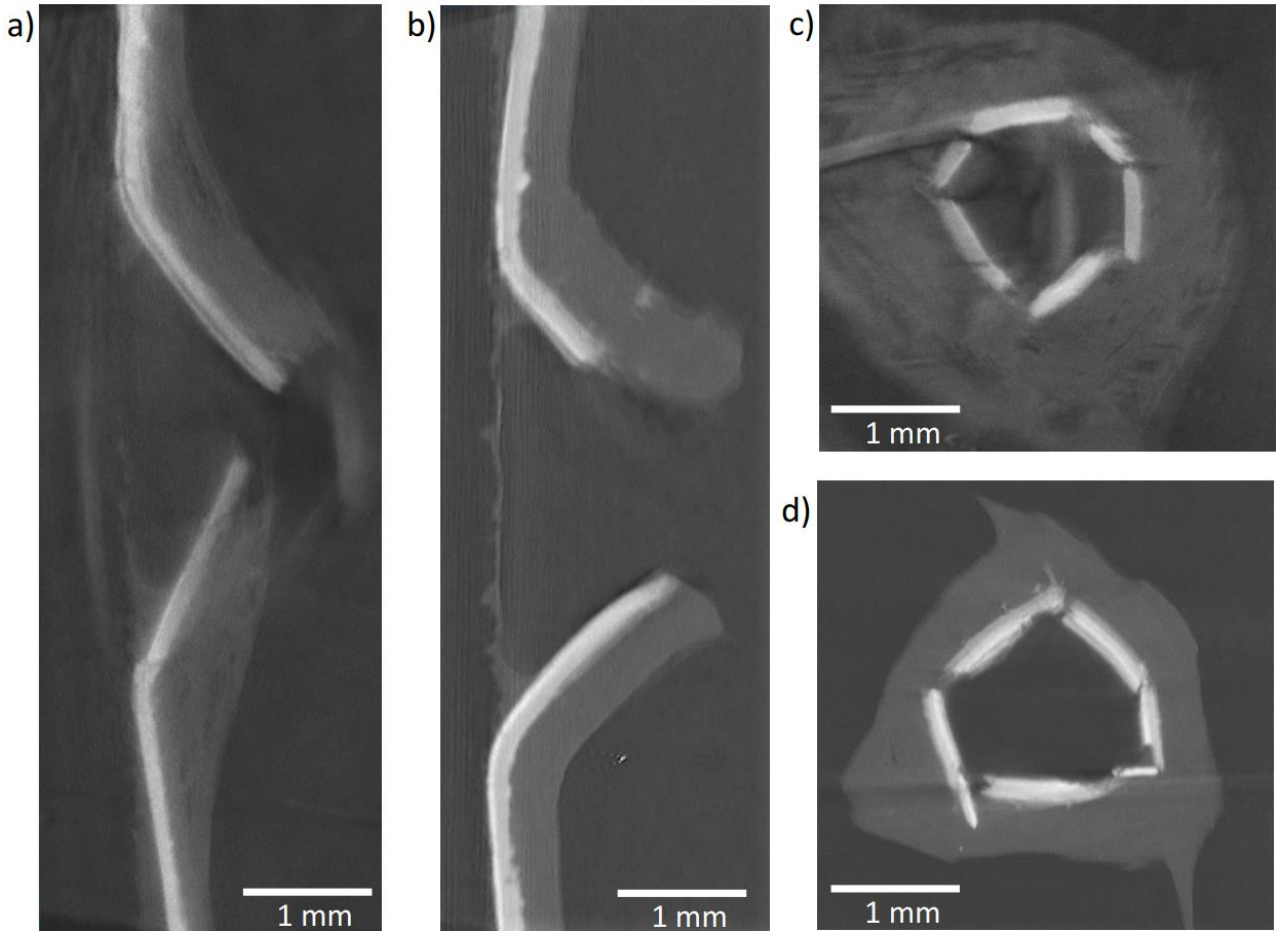

Figure 3.6. MicroCT scans of selected representative scales of from the head region after transverse puncture loading at 50 mm/s a) and b) cross-sections at the center of puncture for a hydrated and ethanol treated scale, respectively. c) and d) in-plane views within the internal elasmodine (near the exit of penetration) for a hydrated and ethanol treated scale, respectively.

3.5 DISCUSSION

Elasmoid fish scales are composite laminates consisting of an assembly of plies of unidirectional type I collagen fibrils arranged with a twisted-plywood stacking sequence. Their primary function as dermal armors is to provide resistance from physical threats without encumbering locomotion. Although these materials were not designed by engineers, they are

certainly advanced in light of their hierarchical microstructures and performance [Yang et al., 2013a]. In this investigation, elasmoid scales of the carp were exposed to a polar solvent to explore the importance of comparatively low-energy secondary bonds (i.e. hydrogen bonding) within and between the collagen molecules and the interfaces of individual plies, to the strength and toughness. The importance of interface mechanics on the mechanical behavior of natural materials was recently highlighted by Barthelat et al. [2016]. The present findings provide a unique and complimentary contribution by showing the capacity for tuning the interface properties through molecular bonds and the corresponding improvements in structural behavior.

Considering the predator and prey relationship for fish, most forms of attack would involve puncture and at high loading rates. The influence of loading rate on the elastic behavior of scales was investigated by Lin et al. [2011], whereas other aspects have received limited attention. Ghods et al. [2017] recently showed that under dynamic loading the layered microstructure of fish scales is more effective at resisting failure by transverse impact than in-plane tension. Furthermore, the laminated structure of the scales exhibits spatial variations in structure and mechanical behavior across the body. Scales from the head region achieve the greatest resistance to puncture, which results from the larger percentage of mineralized layers of the elasmodine in comparison to the middle and tail regions. After exposure to ethanol, scales from the head region were also the most resistant to puncture, and over the entire range of strain rates (Figure 3.4). Nevertheless, the greatest increase in the load and work to failure after exposure to ethanol was achieved by scales from the tail region (Figure 3.5).

As evident the stress-strain responses in Figure 3.1, the scales undergo a form of strain hardening with deformation. Chintapalli et al., [2014] commented on the strain hardening characteristics of biological composites, and that natural materials rely on strain hardening to

maintain their functionality and tolerate defects and damage. In most mineralized structural materials, the strain hardening response is restricted to the interfaces between highly mineralized components that are mediated by connective proteins. However, apart from the LL, the composition of elasmoid scales is dominated by the collagenous proteins of the fibrils, as well as the connective organic elements at the interface of the fibrils and the lamina. That increases the capacity for strain hardening. Strain hardening can also result from the inherent resistance of the individual lamina to rotation and sliding about the interfaces in response to the orientation of Mode I loading. Scales from the tail region underwent the greatest extent of strengthening overall, and in both the water and ethanol conditions. Due to the lower relative mineral content of scales from the tail region [Murcia et al., 2016], the intra-and interfibrilar mineral appears to temper the effectiveness of the strengthening mechanisms in this highly organic system when considering the strain rate behavior.

The extent of strain hardening in the tensile response of the scales was dependent on the rate of loading and environment (Figure 3.1). Both the strength and toughness of the scales increased with strain rate. Exposing the scales to ethanol increased the extent of strain hardening, which was further amplified with increasing strain rate. Indeed, after exposure to ethanol the strain rate sensitivity exponents for the tensile strength increased by 30 to 50% with respect to those values for the scales in water. Mechanistically this in interpreted to result from the increased resistance to interfacial sliding posed by the newly formed interpeptide and interfibrillar hydrogen bonding within and between fibrils. In the hydrated condition, the water molecules serve as a molecular lubricant to facilitate sliding. When replaced with ethanol, the ethanol molecules are retained within and about the collagen fibrils. That reduces the extent of shrinkage in comparison to air

drying, and reduces the potential for interfacial friction to be a predominant factor contributing to the increased resistance to deformation.

Contributions from molecular-scale and ply-level mechanisms to the strain hardening response of the scales during inelastic deformation are rather easy to conceive. But what quality or mechanism is responsible for the strain rate sensitivity in the scales? The principal constituent is collagen, which undergoes an increase in resistance to deformation with increasing strain rate [Arumugan, et al., 1992; Shergold et al., 2006; Zhou et al., 2010]. The next contribution is potentially at the interface of the individual plies. The Bouligand-type structure of scales allows the lamina to undergo rotation according to the loading orientation [Zimmermann et al. 2013] and reorientation along the tensile axis. That process promotes interfacial sliding and stretching of the connective proteins that exhaust mechanical energy [Yang et al., 2014]. These proteins are also rate sensitive. Therefore, it is the strain rate sensitivity of the proteins that are reflected in the macroscopic response.

The strain rate sensitivity exponents for tension and puncture were nearly equivalent ($m \approx 0.1$) in water. But ethanol treatment caused an interesting change. Under tension, the strain rate sensitivity increased with ethanol treatment by at least 30%. That suggests that the interpeptide hydrogen bonds stimulated by the removal of water are more rate sensitive than the hydraulic processes activated by the displacement of free and bound water with deformation, and the inherent rate sensitivity of the tropocollagen molecules without interpeptide hydrogen bonds. These mechanisms contribute to the global deformation that occurs during tensile loading of the samples.

Contrary to the increase in rate sensitivity in tension, the ethanol treatment caused a decrease in m for the puncture responses by approximately 50%. According to a review of the dynamic behavior of layered biological materials [McKittrick et al., 2010], energy dissipation occurs

principally via mechanisms operating at the micro-scale, including delamination and microbuckling of the lamella. The dissipated energy increases with the extent of new surface area generated. After exposure to ethanol, the μCT scans (Figure 3.6d) showed the delaminated zone was smaller, which must result from the increase in interfacial bond strength due to the hydrogen bonding, and the large stress gradient under puncture loading. That resulted in suppression of the zone contributing to energy dissipation overall, and the effect of interfacial processes to the rate sensitivity. In addition, the limiting layers plays an important role in the puncture resistance, which is in influenced less by the polar solvent due to the low volume fraction of collagen. Admittedly this interpretation is speculative, and further work is required to understand the contributing mechanisms more clearly.

One interesting aspect of the responses to tension was that the strain to failure increased with strain rate until reaching a plateau at approximately 10 s^{-1}, and then decreased significantly with higher rate (Figure 3.2c). In water, the strength and toughness also decreased with strain rate >10 s^{-1}. Bone undergoes a ductile to brittle transition at moderate to high strain rates that are very similar to the range noted in the scales Hansen et al., [2008]. While exposure to ethanol had almost no influence on the strain to failure, it promoted strengthening and increased toughness over the entire range of strain rate (Figure 3.2b and 3.2d). Most mineralized tissues undergo reductions in strength and toughness with dehydration in air [Evans and Lebow, 1951; Kahler et al., 2003; Bajaj et al., 2006; Yan et al., 2008; Nyman et al., 2013] and even in ethanol [Lucksanasombool et al., 2001; Nalla et al., 2005]. Johnson et al. [2017] recently presented results on the strain-rate characteristics of the bighorn sheep horn keratin in both hydrated and dehydrated conditions. While the strength increased with strain rate in both tension and compression, there was a decrease in toughness, which appeared to be due to the reduction in strain to failure with dehydration. In

contrast, Torres et al [2015] reported on the impact resistance of scales from the Arapaima Gigas under charpy testing in both hydrated and dehydrated conditions. In that study, the energy to fracture of the dehydrated scales exceeded that of the hydrated condition by 2X or more. Thus, interpeptide hydrogen bonding is effective at resisting the embrittlement that occurs with increasing strain rate, but it appears limited to systems with lower mineral content. In essence, the mineral interferes with the molecular bonding that is essential for this mechanism of toughening.

The dynamic response of engineered composites to axial and transverse impact loading is of substantial importance. In these materials, an increase in stiffness with strain rate is common, but generally limited to factor of 2X, which is substantially less than that of the scales (Figure 3.2a). For carbon/epoxy composites, the strain rate sensitivity is largely based on the resin properties, as expected, but is also dependent on the stacking sequence [Hsiao and Daniel, 1998; Gilat et al., [2002]]. And while an in increase in stiffness with strain rate is common, the change in toughness is dependent on the constituents. An excellent review of the strain rate effects on the mechanical properties of composite materials was presented by Jacob et al. [2004]; efforts concerning the impact resistance of engineered composites are largely focused on the extent of delamination. In an evaluation of various textile composites for impact resistance, Flanagan et al. [1999] highlighted that stacking/blending layers with unique material characteristics (e.g. Spectra/aramid) improved the energy absorption as well as the material structural integrity at the interfaces. One aspect of the scale responses that was not considered in detail was the role of the highly-mineralized limiting layer, as well as the interface between the EE and IE in the impact responses. Clearly this is an area that requires further consideration. Overall, the reduction in damage zone that resulted from ethanol exposure suggests that there are additional inspirational qualities of scales to explore.

The findings of this investigation advance our understanding of the mechanical behavior of this unique class of composite materials. Nevertheless, there are some recognized limitations to the investigation that are important to consider. For instance, although the armor of fish involves an assembly of imbricated scales and skin, the experiments were focused on the properties of individual scales, and not multiple scales. Previous work under quasi-static loading showed that the stacking of elasmoid scales amplifies the overall puncture resistance [Khayer et al., 2013], and is important to the strain-stiffening response of scaled skins [Vernerey and Barthelat, 2010]. Stacked scales or the skins may exhibit different behaviors. Similarly, the puncture loading was performed on scales restrained by peripheral clamping, and not on a compliant backing that simulates the fish body. Although the work of Khayer et al., [2013] did not find contributions from the compliant substrate backing to the puncture resistance of fish scales, it could be important to the type of damage incurred to the fish (contusion rather than puncture). An additional concern is that experiments were limited to the scales of the carp. That is important for two reasons, including i) the differences in number of mineralized plies, which would change the EE ratio, and ii) the difference in lamination and relative ply orientations [Murcia et al., 2017]. Rotation of the individual lamina in response to the opening mode stress is a primary contribution to the toughness of scales [Zimmermann et al., 2013; Yang et al., 2014]. As such, differences in the stacking sequence of plies and their orientations could contribute to the strain-rate response of these materials.

Another limitation to consider is related to the mechanism of toughening that results from exposure of the scales to ethanol. An increase in resistance to failure was observed after exposure to ethanol, and is speculated to originate from interpeptide bonding within and between the collagen fibrils. This increased degree of bonding would act to suppress delamination between

fibrils, as well as between plies. If stretching and sliding of the lamina relative to one another is an important contribution to the global deformation [Zimmermann et al., 2014], then molecular bonds that resist that process should be beneficial. Indeed, there was evidence that delamination was suppressed in the μCT images of the punctured scales subjected to ethanol treatment (Figure 3.6) with respect to those evaluated in water. Nevertheless, the increase in hydrogen bonding was not quantified, it was only deduced from the increase in stiffness (Figure 3.1). Related to this concern, only one polar solvent was used. The effectiveness of polar solvents to form hydrogen bonds in collagen is often described in terms of the Hansen solubility parameter for hydrogen bonding. Polar solvents with high values, like water, preferentially form hydrogen bonds with collagen peptides, thereby preventing the molecules from developing interpeptide bonds. When the water is displaced by a polar solvent with lower solubility parameter than that of collagen in air (e.g. ethanol), interpeptide hydrogen bonding occurs. Therefore, it would be possible to evaluate the importance of this bonding on the dynamic response of these fibrous composites through the use of polar solvents with different solubility parameters. The value of this effort is in using the microstructure of these natural composites to discover new ways to amplify the impact resistance or engineered composites utilizing secondary reversible molecular bonds. That exercise is reserved for future study.

3.6 CONCLUSIONS

An experimental investigation on the dynamic loading responses of a natural laminated composite (elasmoid fish scales) was conducted that involved both in-plane axial tension and transverse puncture loading to failure. Scales were obtained from three different regions of multiple fish, including near the head, middle and tail, and then evaluated as fully hydrated (in

water) or after exposure to a polar solvent (ethanol). There was a significant increase in the resistance to failure with rate of loading for both loading orientations, and the largest resistance to failure overall resulted from the scales exposed to ethanol. The strain rate sensitivity exponent in tension increased by up to 50% after exposure to ethanol, but decreased in transverse puncture loading by as much as 70%. The largest strength and toughness in tension, as well as the largest load and work to puncture were obtained by scales from the head region of the fish, which is attributed the greater proportion of mineralized layers in those scales when compared to the middle and tail regions. Nevertheless, the largest increases in the resistance to failure with loading rate occurred for scales of the tail when exposed to the polar solvent, with up to 7X increase overall in the work to puncture. The toughening caused by intermolecular hydrogen bonding in the presence of ethanol was most effective in the scales of the tail due to the lower mineral content and reduced interference caused by the mineral reinforcement. Results of this investigation underscore the importance of weaker interfibril bonding on the mechanical behavior of these natural laminated composites and signify the potential for pursuing bioinspired material designs with substantially greater impact resistance based on this concept.

Chapter 4. DEVELOPMENT OF BIOMIMETIC SYNTHETIC COMPOSITE MATERIALS INSPIRED BY ELASMOID SCALES

4.1 SYNOPSIS

As established in Chapter 3, the introduction of interpeptide bonding within and between the collagen fibrils caused a substantial change in the mechanical properties of the scales. This treatment significantly enhanced the strength and the overall toughness of the material. In addition, there were spatial variations in the properties of the scales between the head, middle and tail regions, which were perceived to result from the differences in mineral content between scales of these three regions. The higher mineral content of the EE in scales of the head region resulted in greater stiffness and strength, as well as greater toughness. That suggests that one approach for pursuing biomimetic improvements in composites in general, and the develop of bioinspired armors in particular, is to selectively reinforce a polymeric fiber system. In this phase of work a commercial UHMW-PE fiber composite was selectively reinforced with alumina particles over a range of areal densities. The resulting changes in mechanical behavior were evaluated in terms of the transverse puncture resistance. It was found that the addition of reinforcement resulted in an increase in normalized work to failure (by thickness) of up to nearly 50% with respect to the unreinforced composite system. Overall, the alumina reinforcement resulted in significant improvements in mechanical behavior with minimal thickness and weight increases. However, the increase in work to fracture resulted from the development of new surface area and an increase in damage area, in contrast to the changes achieved by the polar solvent treatment.

4.2 MATERIALS AND METHODS

Many polymer fiber composites exist, with polyaramids and ultra-high molecular weight polyethylene (UHMW-PE) being among the most common. Both are already in use for armors, which makes any improvements more readily beneficial for future armor material designs. In this phase of the investigation, novel composites were developed using commercially available alumina powder and a commercial fibrous UHMW-PE. The material selected was HB 2 of Dyneema™, which is a "High Ballistic penetration resistant" grade. The material used is a four-ply prefabricated cross-ply laminate of uniaxially aligned Dyneema fibers consolidated by a sparse polyurethane matrix (HB designation and Dyneema are trademarks of Koninklijke DSM N.V.). The method of processing for this material can be seen in Figure 4.1. The laminates were produced with a specific layup by laminating sheets of the cross-ply lamina and subjecting the material to a cure cycle achieved by a hot press. The hot-pressing cycle is stipulated by the manufacturer and followed the cure cycle outlined in Figure 4.2. The cure cycle was achieved using the commercial hot press (Wabash MPI, Model G50H-24, Wabash, IN) in the Mechanical Engineering department at the University of Washington. The maximum load for the hot press was 50 tons, so the surface area of composite was selected to not exceed the maximum pressure. The fabricated composites were cut after the hot press cycle into 50 x 50 mm square test specimens using a straight edge razor blade.

To explore the influence of aluminum reinforcement, areal densities of 50 to 750 g/m^2 were explored with 50 g/m^2 increments. The alumina reinforcement consisted of crushed particles with average effective diameter of 25 um. The reinforcement particles were distributed evenly between two sheets of the premade HB2 UHMW-PE prior to the hot press cycle.

The fabricated composite samples were tested using the same load frame and custom puncture fixture designed for evaluation of the fish scales described in Chapters 2 and 3 (Model ELF 3300, BOSE, Eden Prairie, MN, USA). Two additional 6.3 mm thick steel plates were added to reinforce the clamping portion of the fixture and prevent errors associated with compliance. In addition, a shorter puncture needle was manufactured with respect to that used for evaluating the scales to prevent buckling of the needle under the higher puncture loads; the puncture needle has the same tip geometry as that used for testing of the fish scales. The remaining dimensions and test parameters were kept consistent with previously stated methods in the prior chapters. A loading rate of 50 mm/s was used for all transverse loading tests, which is the fastest rate used in evaluations of the fish scales. Also consistent with evaluating the scales, the puncture load and displacement were monitored, and then used to determine the load to puncture and work to puncture. The addition of reinforcement resulted in an increase in thickness. Therefore, the results were also normalized by thickness to obtain an alternate form of assessment.

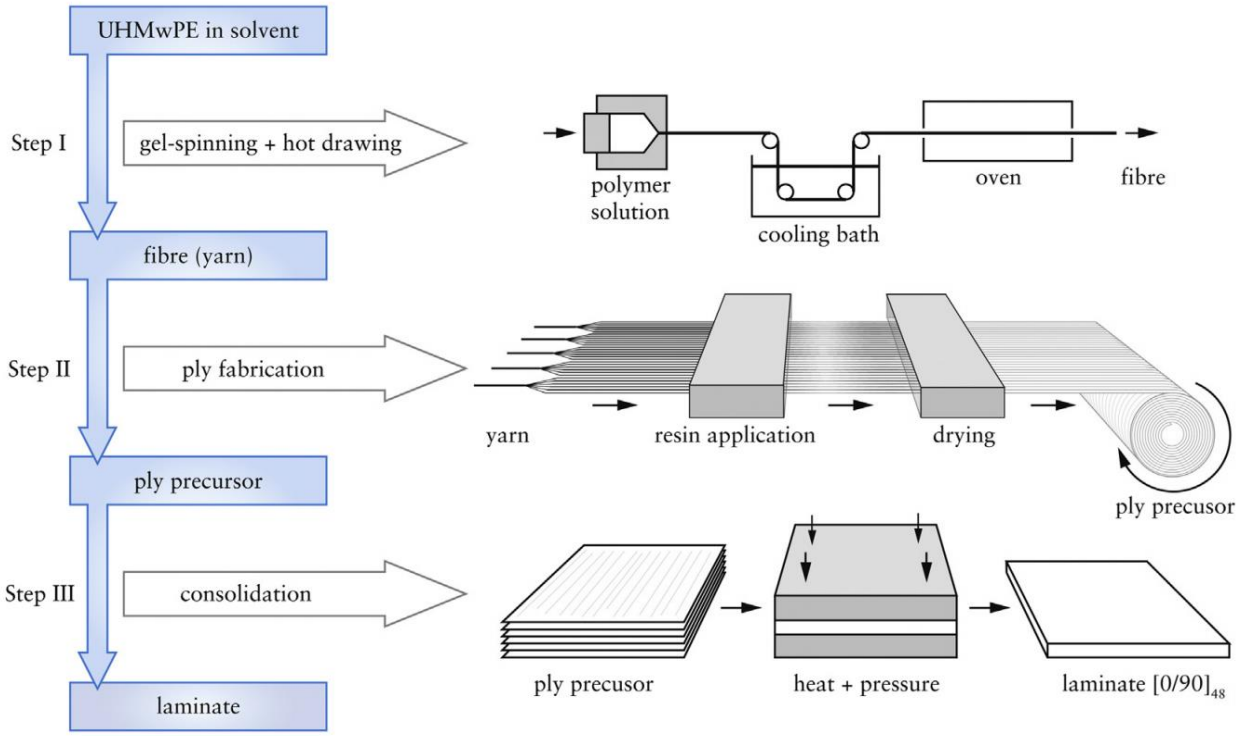

Figure 4.1. Processing of the Dyneema^{TM} UHMW-PE from the precursor polymer solutions to the hot pressing of premade plies. For HB2 four plies of the ply precursor are formed together with a continuous polyurethane matrix. [Russell et al., 2013]

Scanning electron microscopy (JEOL, Model JSM- 6010PLUS/LA, Peabody, MA) was performed to investigate the dispersion of the particulate through the thickness of the Dyneema plies. This analysis was conducted on four of the areal weights at the extremes and two intermediate amounts. Micro Computed Tomography (MicroCT) scanning was performed using a commercial instrument (North Star Imaging X5000) on several samples to obtain an additional view of the particle dispersion and to examine the delamination within the fabricated composites prior to puncture. Scans were typically performed with 50 kV and 1000 uA, 1 frame/sec step scan mode with 10 ms delay, 900 projections, and two frame averaging. However, some of these parameters were slightly modified in subsequent scans to optimize the gray value contrast obtained. Post processing was performed with a proprietary software (efX-CT, Version 1.6, North Star Imaging, Rogers, MN, USA) provided with the microCT instrument.

After identifying the optimal density of particle reinforcement, additional testing was conducted involving the addition of an uniform areal density of alumina to multiple layers. This was performed to investigate the scaling effect, advantage of different stacking sequences, and to investigate ideal location of reinforcement. These composite samples were also loaded at 50 mm/s in the same puncture fixture with 5 samples for each layering sequence. A failed specimen from each of the set of samples was scanned with the microCT to evaluate the extent of damage effects and how it compares to the unreinforced Dyneema composites.

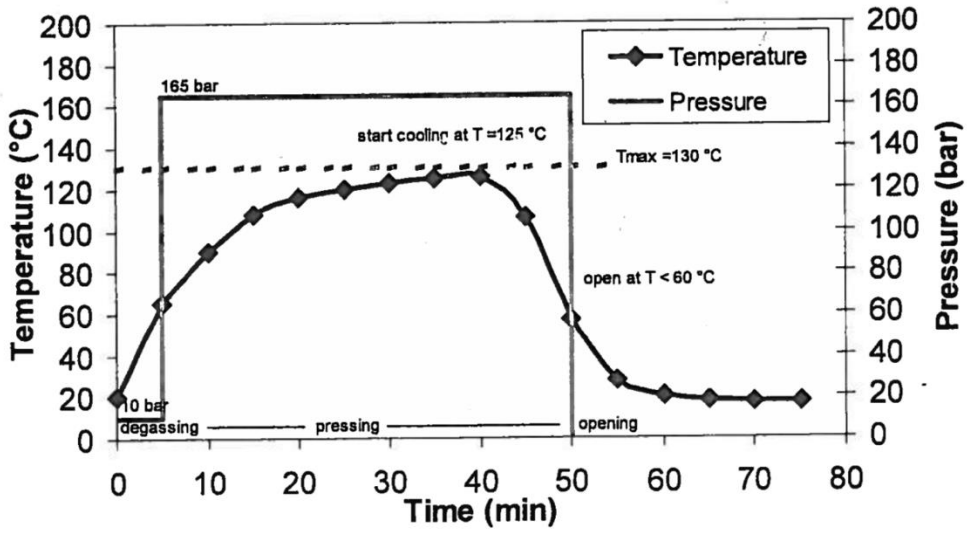

Figure 4.2. Compression mold cure cycle for HB2 and HB25 plate composites. Obtained from the DSM HB2 product specification outline.

4.3 RESULTS

Puncture load-line displacement responses for all of the investigated areal weight density reinforcement conditions are presented in Figure 4.3, along with the results for an unreinforced sample. General trends are evident from a comparison of these load-displacement curves. The metrics used to quantify the puncture resistance from these tests include the stiffness, maximum load to failure, and work to failure as defined from the area under the load-displacement curves to the maximum load. These properties are defined in Figure 3.4. listed in Chapter 3. As evident in Figure 4.3, the maximum load to failure increased with areal density of the alumina particulate reinforcement. The displacement to the maximum load is consistent for all areal density reinforcement conditions. The increase in load and negligible changes in the displacement to maximum load results in an increase in the work to failure with increasing area density reinforcement. Initially, single tests were performed in combination with qualitative SEM analysis

to find a reasonable upper areal density limit. From that analysis, 150 g/m^2 was chosen since it was the highest density with minimal delamination from processing.

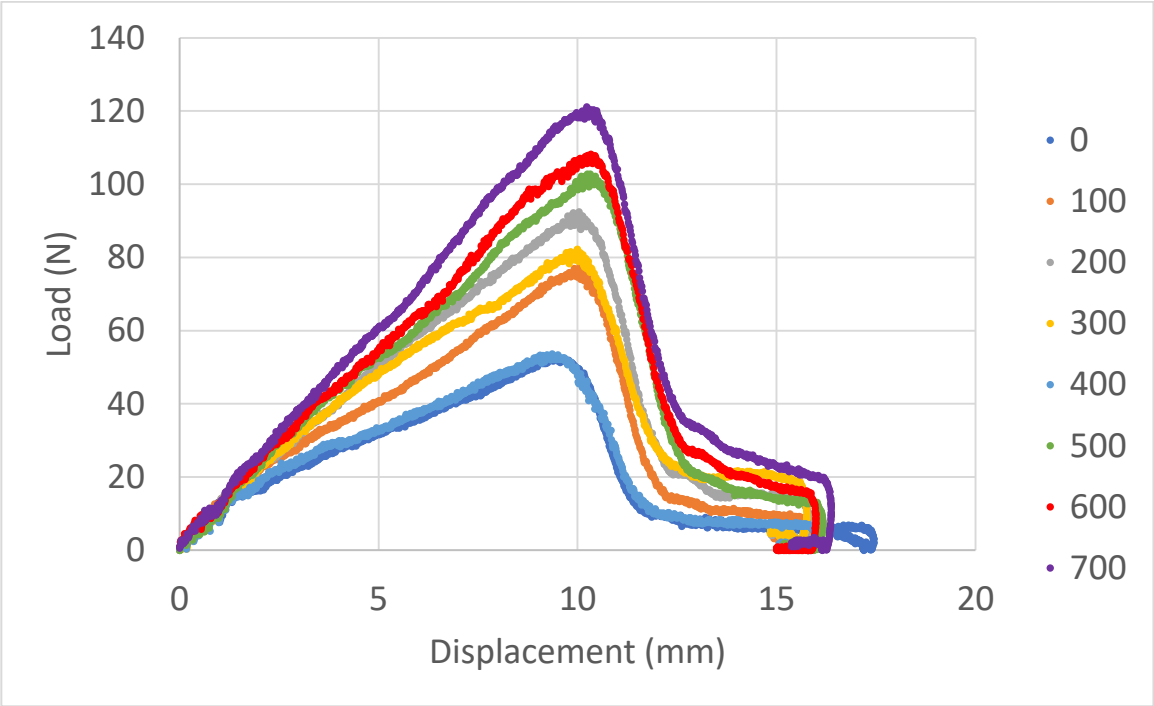

Figure 4.3. Puncture load-line displacement curves for alumina particle areal densities at 100 g/m^2 increments, starting with no reinforcement.

The normalized magnitudes of max load and work to failure for composites designed with multiple layers of 150 g/m^2 are presented in Figure 4.4(a) and 4.4(b). All responses are normalized by the thickness of the specimen. The normalized maximum load to failure undergoes a non-linear increase with number of reinforced layers. Adding the third layer improved the response beyond the approximate linear proportionality established for the prior two layer configurations. The work to failure shows a similar trend with the largest amplification in load and work to puncture occurring with addition of the third layer of reinforcement.

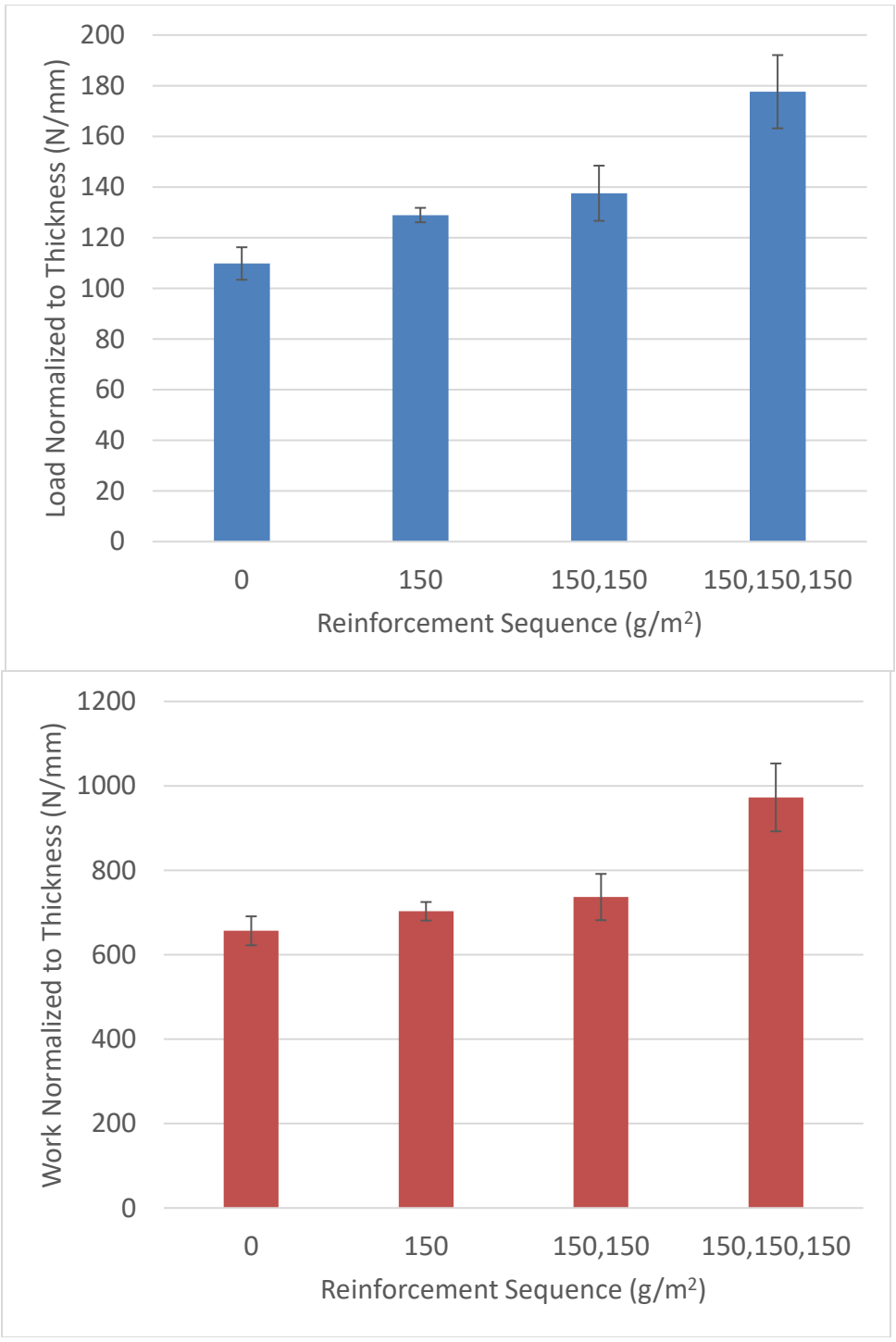

Figure 4.4. Max load to failure (top) and work to failure (bottom) normalized to the thickness of the composites. "0" designates the average of unreinforced two 4 ply layers, "150" is a single layer of 150 g/m^2 in between the two 4 ply HB2 precursors, "150, 150" implies an extra layer of reinforcement and a 4 ply on top, and so on.

The increase in thickness, max load to failure, and work to failure are plotted in Figure 4.5 in terms of the percentage changes. The same naming scheme is used to describe the composite laminate layup as used in Figure 4.4. The thickness increases linearly with number of reinforcement layers, which is expected. The normalized max load increases by roughly 17, 25, 62, and 64 % for single, double, triple, and sequenced layer reinforcement, respectively. The normalized work to failure undergoes an increase of 7, 12, 48, and 49 %, respectively for the same reinforced composites.

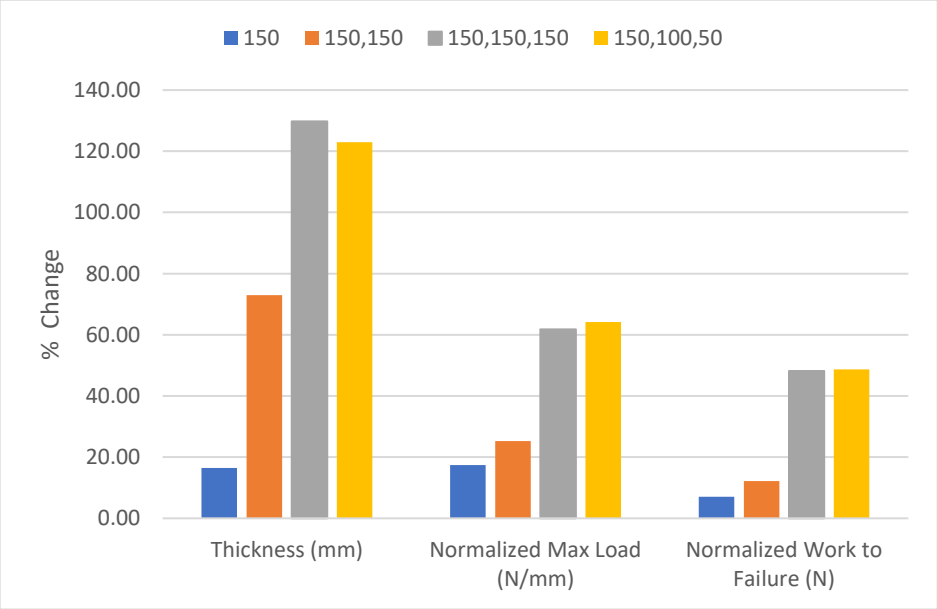

Figure 4.5. Percent changes compared to the unreinforced HB2 for the thickness, max load to failure, and work to failure. "150, 100, 50" implies a reinforcement stacking sequence with 50 g/m^2 between the bottom two layers of HB2, then 100 in the middle, and 150 g/m^2 between the top two layers.

The damage introduced within the reinforced composites as a result of puncture can be seen in the Figure 4.6. These images were obtained from microCT scanning; the bright regions are alumina particulates, the gray is HB2, and the black regions are the delaminated regions of the samples. In

Figure 4.6a, a few distinct damage mechanisms are evident. Specifically, delamination occurs preferentially along the plane of the reinforced interface. Fibers oriented towards the center of the biaxial bending load underwent elongation as a result of the tensile stress and then appear to have recoiled after undergoing failure. There is a minor extent of delamination evident in the layers between the plies of the HB2 laminates. In Figures 4.6b and 4.6c showing the 2 and 3 interface layers of reinforcement, similar mechanisms of energy dissipation involving delamination along the alumina reinforced interfaces and fiber elongation are evident. Figure 4.6c has less delamination evident at the left-most layer of reinforcement, implying that the lower areal density of 50 g/m^2 improves the interfacial strength and reduces propensity for delamination.

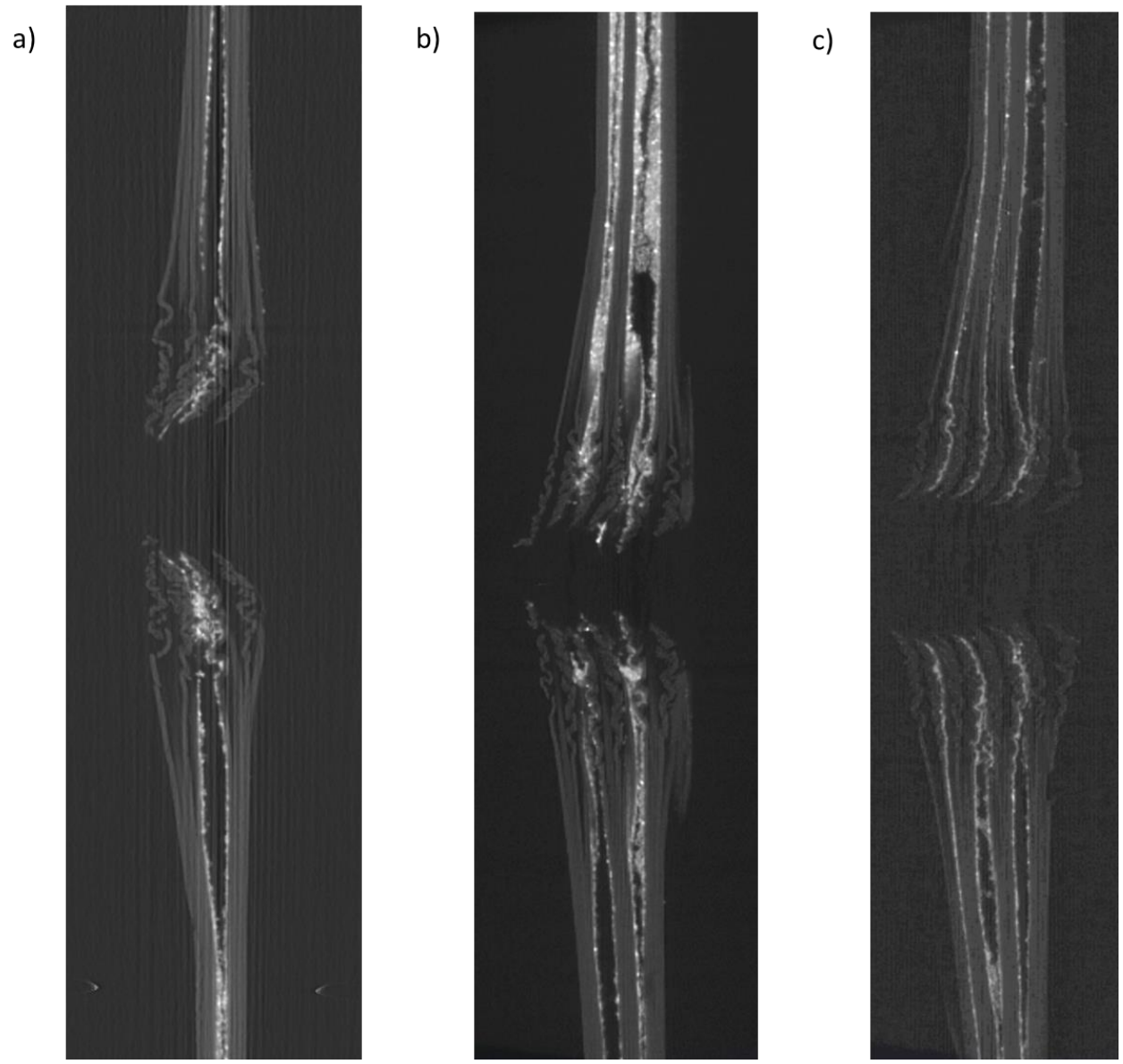

Figure 4.6. X-ray microCT cross-sectional images at the center of puncture for (a) “150”, (b) “150, 150”, and (c) “150, 100, 50”. The direction of puncture is from right to left so the top of the specimens is on the right.

4.4 DISCUSSION

Previous research has shown that UHMW-PE fibrous laminates are a high performance polymeric composites that demonstrates properties ideal for use in ballistic resistance [Russell et al., 2013; Hudspeth et al., 2012; Greenhalgh at al., 2013; O’Masta et al., 2014; Nguyen et al., 2015;

Dingenen, 1989]. These materials are commercially available, and can be used to develop the desired laminations through compression molding of multiple layers. This work attempted to increase the material's resistance to puncture through the addition of sparsely distributed ceramic particle reinforcement.

Based on results of the experiments, the puncture resistance of the UHMW-PE composite can be increased by the addition of micro-particle reinforcement. However, there appears to be a limit to the amount of reinforcement that can be introduced into the HB2 that promotes an increase in puncture resistance. One limitation is that the tightly packed arrangement of fibers in the cross-ply orientation prevents dispersion of the micron scale alumina particles. Figure 4.7(a-d) shows the dispersion of the alumina particles from the interface of the laminate structure from 50 to 700 g/m^2 areal densities. In the first image of the laminate with 50 g/m^2 reinforcement, the reinforcement particles are integrated within the surrounding UHMW-PE fibers to the point where the interface is almost indistinguishable from the other unreinforced layers. For the 250 g/m^2 areal density, the interface is clearer, and a thin layer of alumina particulate is evident. However, the interface still appears intact. The composites with higher areal densities of 500 and 750 g/m^2 exhibit thick layers of alumina particles that prevented consolidation of the two HB2 precursor layers. These did not delaminate fully until after puncture which resulted in complete separation of the layers.

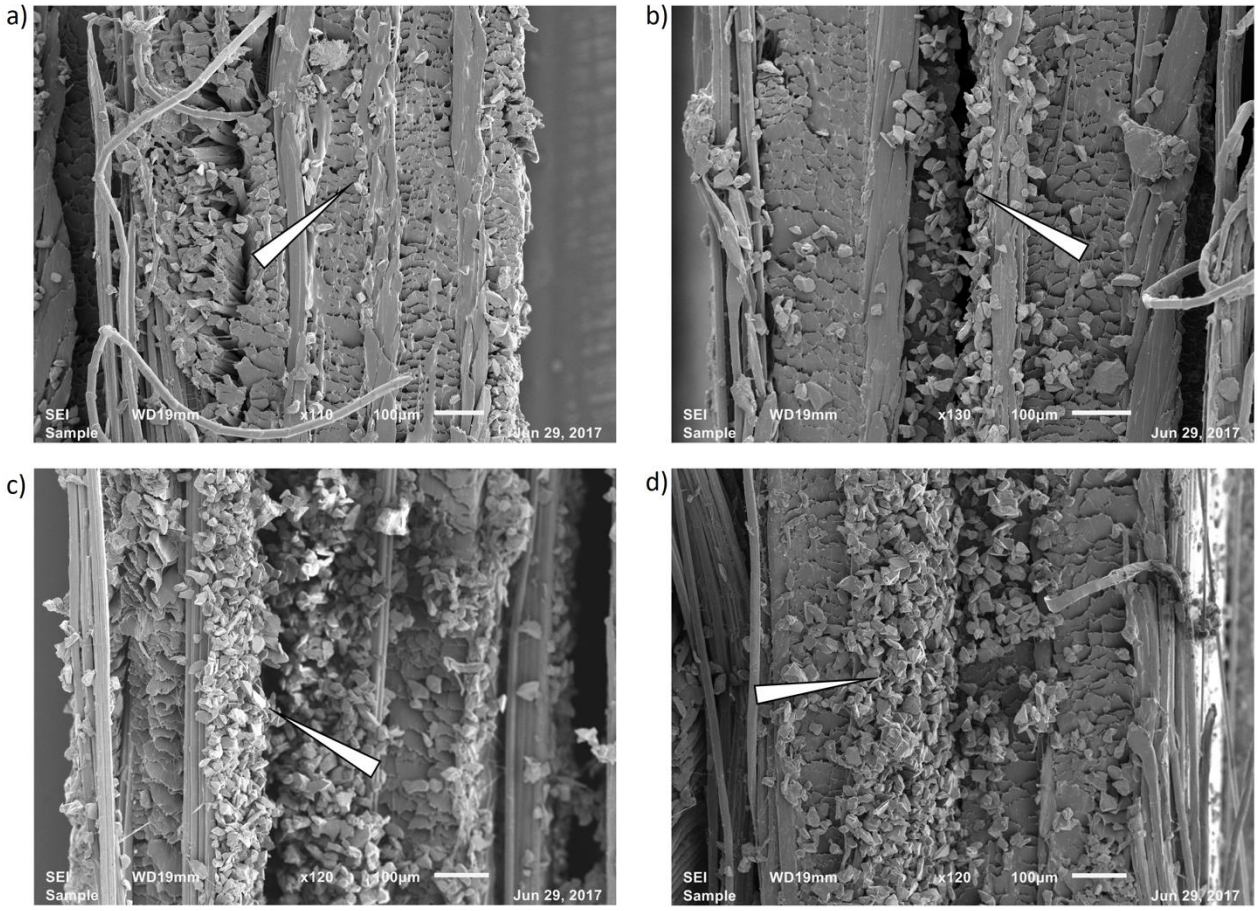

Figure 4.7. SEM micrographs of the composite cross-section for (a) 50, (b) 250, (c) 500, and (d) 700 g/m^2. The white arrow designates the interface where the alumina particles were applied.

Even at the areal densities of 150 g/m^2 and lower, partial delamination occurred at the reinforcement interface during cutting of the samples (Figure 4.8). This implies that the reinforced interface of these composites is fragile even "as fabricated", which should be considered in future efforts. In addition to the delamination, there is a clear discrepancy in the particulate distribution throughout the interface. Nevertheless, the consistency in puncture responses with replication imply that the errors promoted by non-uniform particle distributions was not necessarily as pronounced as the microCT images imply. An improvement in the placement of the powdered alumina could yield better results and potentially eliminate delamination, even at the 150 g/m^2

reinforcement density, since the edge has a greater portion of the particulate that increases the likelihood of delamination with lower loads.

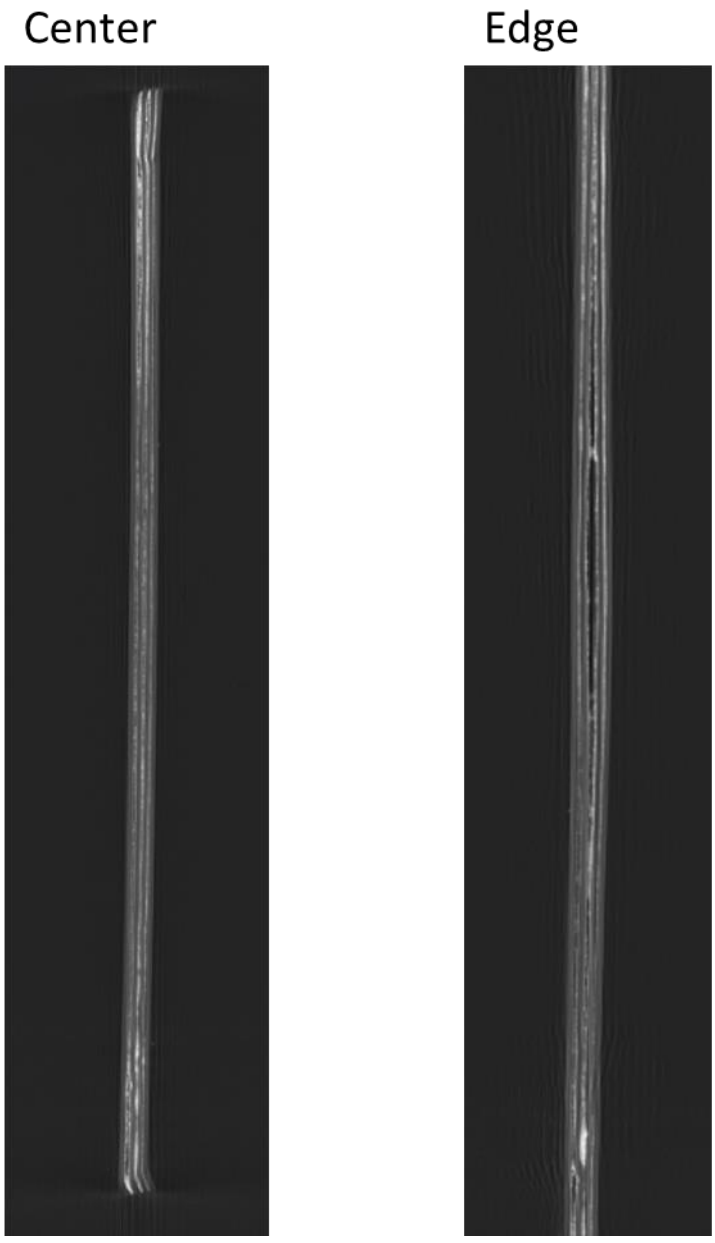

Figure 4.8. X-ray microCT cross-section images of triple layer 150 g/m^2 at the center and the edge of the specimen after specimen preparation and without puncture testing. Delamination is evident near the sectioned edge.

When reviewing the mechanical performance of the reinforced composites in Figures 4.3 through 4.5, the maximum load and work to failure increased with area density of reinforcement, even when normalized to thickness. Clearly the reinforcement presents a distinct benefit. Furthermore, increasing the number of layers of reinforcement further improved the performance. The increase in work to failure most likely results from the additional energy dissipation promoted by interfacial delamination. Weakening the interface between some of the layers allowed cracks to propagate preferentially down these planes. This is analogous to the hydrated fish scales investigated in Chapter 2 and 3, where the hydration disrupted interfibril bonding and lowered interfacial strength between fibers and layers. Delamination allowed these scales to achieve increased energy dissipation at the cost of large damage zones, particularly for scales of the head region, which possessed greater mineral content overall due to larger EE. The same mechanism appears to be contributing for the alumina-reinforced UHMW-PE.

Hot pressing of this material consolidates the uniaxially aligned fibers by creating interfacial mechanical interlock. Evidence of brinelling was reported in this material system, as shown in Figure 4.9, and explains one contribution to the resistance to delamination that the HB2 has even with minimal matrix material [Russell et al, 2013]. This deformation of the fibers allows for increased surface area contact and larger degree of interfiber van der Waals bonds [Karbalaie et al., 2011]. Having particle reinforcement would be expected to offset a portion of this brinelling and interfiber contact, which explains the weaker interface and delamination observed. However, that does not explain how the reinforcement is improving the maximum load to puncture.

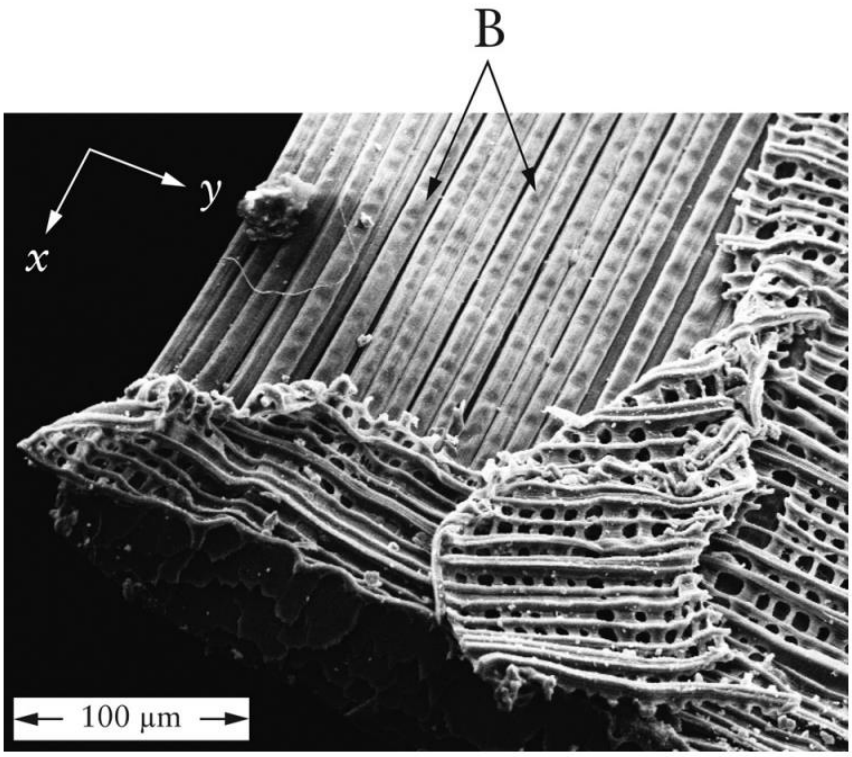

Figure 4.9. SEM micrograph showing the brinelling that occurs in hot pressed UHMW-PE composites after Russell et al. [2013].

Another interesting finding is the greater increase in resistance to puncture of the three layer 150 g/m^2 and "150, 100, 50" composites. This may be a result of some intrinsic benefit of adding more reinforcement or distributing the additional reinforcement over a greater number of layers. However, this may come from a ply number effect. Greenhalgh et al. [2013] recently evaluated the failure process of UHMWPE consolidated plates subjected to ballistic impact. Layers closer to the point of impact experience very localized stress that cause the material in front of the bullet to nearly disintegrate. As energy is dissipated by deformation and the creation of new surface area, the lower layers work to trap the projectile and transfer load along the fibers through tension. At this point a combination of tension, interfacial shear, and delamination take place. There is an apparent thickness effect at play in UHMW-PE fiber composites for ballistic

impacts [Greenhalgh et al., 2013; Nguyen et al., 2015]. This combination of deformation modes with increasing thickness change can provide explanation for the nonlinearity in impact resistance increases of the reinforced HB2 with increasing thickness (Figure 4.4).

In the testing performed in this thesis the indenter did not reach ballistic speeds. However, the dynamic speed may be adequate enough to invoke the thickness effect from the thinner to thicker samples. Impact involving higher effective strain rates may further amplify the effect since the mechanics of deformation will change so there is a larger degree of load transferred along the plies that stay intact. While speculative, this is worthy of further study.

If this approach, particulate reinforcement was introduced manually within a commercially available material to improve the impact resistance of UHMW-PE composites. Further work needs to be performed to improve processability. The methods utilized in this investigation were time consuming and difficult to obtain consistent composites. Instead of distributing an array of dry alumina particles, a viscous slurry of alumina could be made. This would allow for the easier and more uniform deposition of a thin layer onto the HB2. However, there may be an issue of volatiles not evaporating and diffusing out of the sample. Better powder deposition could also be pursued, but dry powder prevents any other geometry aside from flat plates. Curvature would cause shift and uneven distribution.

4.5 CONCLUSION

In this chapter, bioinspired composites plates were developed using fibrous UHMW-PE laminates reinforced with alumina particles. Introducing the alumina between selected interfaces of the 4 cross-ply precursor prior to hot pressing promoted improvements in the mechanical performance when compared to the unreinforced Dyneema composite. An amplification of the

impact resistance was seen with increasing thickness. Modulating the amount of reinforcement and distributing the reinforcement through thickness provided additional improvements in impact resistance with lower total weight increase. MicroCT scanning showed that addition of the alumina improved the work to failure largely though delamination of the reinforced interface. This is the opposite of the chemically dehydrated elasmoid scales in Chapter 3, which underwent an increase in the puncture resistance as evaluated by the work to puncture with reduced damage. Overall, the addition of alumina reinforcement, akin to the reinforcement in elasmoid scales of the head region of the carp, provides significant increase in puncture resistance with minimal thickness and weight increases. Assuming it is for single-attack applications, where damage mitigation is not necessary, this composite could excel. Perhaps that is one reason why the scales of fish are capable of regeneration.

Chapter 5. CONCLUSIONS AND FUTURE WORK

5.1 CONCLUSIONS

In this thesis, elasmoid fish scales were evaluated to obtain further understanding of the mechanical behavior of this unique material system, and to apply this knowledge to fabricate new "first generation" materials for flexible armors. The hierarchical structure of scales consists of an organized network of mineralized collagen fibers that presents a unique opportunity for guiding the development of a new category of engineering composites. It is envisioned that emulating the microstructure of elasmoid scales with appropriate choice of engineered materials could result in the development of new materials capable of achieving performance that is superior to those presently used for impact and puncture resistant applications.

The investigation consisted of three major phases. In the first phase, elasmoid fish scales from common East Asian Carp were evaluated under uniaxial tension and transverse puncture loading arrangements. The loading was performed over a large range of strain rates that extended from quasi-static to dynamic conditions. The strain rate sensitivity was determined for several important metrics of mechanical behavior. When assessed in terms of the toughness, the strain rate sensitivity exponents for tensile and puncture loading were 0.10 and 0.35, respectively. Scales are structured to be most effective at protecting fish from transverse impact and puncture under dynamic loading. The high strain-rate sensitivity allows for greater flexibility at low velocities associated with locomotion (relative to impact speeds) and substantially greater energy dissipation when the material undergoes dynamic impact. The higher sensitivity in transverse loading – relative to tension – appears to be associated with the layered structure of the scales and their composition. However, further work is needed to achieve greater understanding of this phenomenon.

In the second phase, elasmoid scales of the carp were subjected to a weak polar solvent (ethanol) to pursue enhancement of the mechanical performance via interpeptide and interfibril bonds. Ethanol has a lower polarity than water, thus making it less likely to bond to polar groups of the collagen peptides, and results in greater hydrogen bonding between fibrils relative to a hydrated environment. It was shown that the ethanol soaked scales outperformed the hydrated scales in both tensile and transverse puncture loading. Across the entire range of strain rates explored, the polar solvent treatment caused substantial increases in all properties with a maximum of 7X increase in the work to puncture of scale from the tail region. However, despite improvements in the individual properties, the treatment caused a decrease in the strain rate sensitivity of the material. Nevertheless, interpeptide bonding induced by exposure to the polar solvents reduced the extent of damage from the focus of puncture. The secondary interfibril bonding apparently increases the interfacial strength between the fibers and the individual plies as well (as shown in microCT analysis). Damage resistance is of significant interest for engineering composites. The findings of this investigation could stimulate new strategies for mitigating damage and maintaining the structural integrity of composite materials subjected to impact loading.

In the third phase of this investigation, a novel composite was developed following the inspiration from some aspects of the fish scale microstructure. In particular, the composite was developed using a combination of a commercial UHMW-PE fiber laminate system reinforced with a distribution of ceramic particulates. Specifically, HB2 4 ply laminates of Dyneema^{TM} were consolidated with varying areal weight densities of alumina powder between the laminates. An evaluation was performed that involved mechanical testing by puncture, SEM, and X-ray microCT analysis to identify the best areal density of reinforcement. Puncture loading was

performed at the highest rate. The resistance to puncture was quantified and the failure mechanisms were qualitatively determined by X-ray microCT. The addition of alumina reinforcement resulted in statistically significant improvements in max load and work to failure. Thicker samples, with more layers and reinforcement exhibited greater improvements, with 7 vs. 48 % increase in the work to failure for single- and three-layer laminates with only 150 g/m^2 reinforcement. Adopting a stacking sequence that mimicked the variation in mineralization through the thickness showed similar improvements to the uniform 150 g/m^2 samples, but with less overall addition of alumina.

Overall, the findings provide additional understanding of the impressive mechanical behavior of elasmoid fish scales and further establish the potential for developing synthetic composites that are guided by the microstructure of scales.

5.2 FUTURE WORK

As with all investigations, there are limitations in time and resources that warrant future work. Many avenues exist for extension of the work performed in this thesis. Regarding the efforts involving fish scales, there is merit for testing with higher velocity since the range in velocity of puncture does not reach those in ballistic events. Extending the range would also allow for a better understanding of the strain rate sensitivity relationship between hydrated and chemically dehydrated scales. Several parts of the studies performed were limited and further characterization could be beneficial. For instance, an analysis of the interfaces after chemical dehydration to reaffirm the theory behind the damage zone reduction would be valuable. A larger sample size would also be valuable to further increase the confidence in the values that were

approaching statistically significance and establish trends in the single sample preliminary areal density testing.

As discussed in the introduction, there are several other aspects of the scale microstructure that appear to be important to the mechanical behavior. Ply stacking sequence and orientations, EE/IE ratio, mineral content, and the LL shape and thickness are a few of the unique structural components of the scales that should be considered in future work. The biomimetic composites that were fabricated in this research only applied two major aspects of the scale microstructure. Namely, polymeric fibers served as the base material and ceramic (mineral) particulate was introduced to reinforce the matrix. This is an essential first step, however there are many directions in which the research can extend. For instance, application of the alumina reinforcement to individual layers of uniaxial UHMWPE could be pursued. The HB2 described in Chapter 4 was a 4-ply precursor that prevented the dispersion of reinforcements through the thickness. Consequently, there was a high concentration of alumina at the applied interface, very little at the next ply and essentially no reinforcement beyond that. The use of smaller particle sizes could help in achieving greater diffusion and potential integration at the interfaces of the fibers themselves. This would be closer to the nanocrystal reinforcement seen in the collagen fibers.

Pursuing ways to emulate the interpeptide bonding achieved by chemical dehydration would be very interesting as well. This could potentially be done by functionalization of the polyethylene to have polar groups. With the close proximity of the fibers, they have a large population of interfaces that could be strengthened with the secondary bonding of the new polar groups. Apart from the alumina reinforcement, this should provide the same benefits as the dehydration of the fish scale, including greater strength, toughness, and reduction in extension of

damage. However, functionalization of the UHMWPE could have inherent drawbacks that would outweigh the secondary bonding provided. The polymer obtains its mechanical properties from the long, high molecular weight polymer chains that are aligned along the length of the fibers. Processing to introduce functional groups like carboxyls could potentially cause chemical degradation though chain splitting.

In addition to opportunities related to the constituents and their interfaces, utilizing hybrid arrangements of materials would be a worthwhile pursuit. For instance, stacking two different composites, such as carbon fiber and UHMWPE, or reinforced and unreinforced UHMWPE, to mimic the EE and IE, would be interesting. Furthermore, modulating the ratio of the synthetic EE and IE as seen in scales across the body of the fish is another opportunity for exploration. Furthermore, ceramic plates could be added to the surface of the synthetic sandwiched materials to imitate the LL. Very limited research has been performed to utilize the microstructural designs of natural materials and biomimetic principles to actually guide the development of new armor materials. With inspiration drawn from elasmoid fish scales, specifically, it appears that there is tremendous possibility for developing new classes of composite materials with improved properties.

REFERENCES

Achrai B, Wagner HD. Micro-structure and mechanical properties of the turtle carapace as a biological composite shield. Acta Biomater. 2013;9(4):5890-902.

Adharapurapu RR, Jiang F, Vecchio KS, 2006. Dynamic fracture of bovine bone. Mater Sci Eng C 2006;26:1325–32.

Allison PG, Chandler MQ, Rodriguez RI, Williams BA, Moser RD, Weiss CA, Poda AR, Lafferty BJ, Kennedy AJ, Seiter JM, Hodo WD, Cook RF. Mechanical properties and structure of the biological multilayered material system, Atractosteus spatula scales. Acta Biomater. 2013;9(2):5289-96.

Arumugam V, Naresh MD, Somanathan N, Sanjeevi R. Effect of strain rate on the fracture behaviour of collagen. J Mat Sci. 1992; 27: 2649-52.

Bajaj D, Sundaram N, Nazari A, Arola D. Age, dehydration and fatigue crack growth in dentin. Biomaterials. 2006;27(11):2507-17.

Barthelat F. Science and engineering of natural materials: merging structure and materials. J Mech Behav Biomed Mater. 2013;19:1-2.

Barthelat F, Mirkhalaf M. The quest for stiff, strong and tough hybrid materials: an exhaustive exploration. Journal of The Royal Society Interface 2013;10(89):20130711.

Barthelat F, Yin Z, Buehler MJ. Structure and mechanics of interfaces in biological materials. Nat Rev Mat. 2016;1(16007):1-16.

Bigi A, Burghammer M, Falconi R, Koch MH, Panzavolta S, Riekel C. Twisted plywood pattern of collagen fibrils in teleost scales: an X-ray diffraction investigation. J Struct Biol 2001;136(2):137-43.

Browning A, Ortiz C, Boyce MC. Mechanics of composite elasmoid fish scale assemblies and their bioinspired analogues. J Mech Behav Biomed Mater. 2013;19:75-86.

Bruet BJF, Song J, Boyce MC, Ortiz C. Materials design principles of ancient fish armour. Nat Mat. 2008;7,748–56.

Buehler MJ. Malecular nanomechanics of nascent bone: fibrillar toughening by mineralization. Nanotech. 2007;18(29):295102.

Chandler MQ, Allison PG, Rodriguez RI, Moser RD, Kennedy AD. Finite element modeling of multilayered structures of fish scales. J Mech Behav Biomed Mater. 2014;375-89.

Chang Y, Chen PY. Hierarchical structure and mechanical properties of snake (Naja atra) and turtle (Ocadia sinensis) eggshells. Acta Biomater. 2016;31:33-49.

Chen IH, Kiang JH, Correa V, Lopez MI, Chen PY, McKittrick J, Meyers MA. Armadillo armor: mechanical testing and micro-structural evaluation. J Mech Behav Biomed Mater. 2011;4(5):713-22.

Chen PY, Schirer J, Simpson A, Nay R, Lin YS, Yang W, Lopez MI, Li J, Olevsky EA, Meyers MA. Predation versus protection: fish teeth and scales evaluated by nanoindentation. J Mater Res 2012;27(1):100-12.

Chen IH, Yang W, Meyers MA. Alligator osteoderms: mechanical behavior and hierarchical structure. Mater Sci Eng C Mater Biol Appl. 2014;35:441-8.

Chen IH, Yang W, Meyers MA. Leatherback sea turtle shell: A tough and flexible biological design. Acta Biomater. 2015;28:2-12.

Chintapalli RK, Mirkhalaf M, Dastjerdi AK, Barthelat F. Fabrication, testing and modeling of a new flexible armor inspired from natural fish scales and osteoderms. Bioinspir Biomim. 2014; 9(3):036005.

Chintapalli RK, Breton S, Dastjerdi AK, Barthelat F. Strain rate hardening: a hidden but critical mechanism for biological composites? Acta Biomater. 2014b;10(12):5064-73.

Currey JD. The design of mineralised hard tissues for their mechanical functions. J Exp Biol. 1999;202(23):3285-94.

Dastjerdi AK, Barthalet F. Teleoast fish scales amongst the thoughest callagenous materials. J Mech Behav Biomed Mater. 2015;52:95-107.

David NV, Gao XL, Zheng JQ. Ballistic Resistant Body Armor: Contemporary and Prospective Materials and Related Protection Mechanisms. Appl Mech Rev. 2009;62(5):050802.

Depalle B, Qin Z, Shefelbine SJ, Buehler MJ. Influence of cross-link structure, density and mechanical properties in the mesoscale deformation mechanisms of collagen fibrils. J Mech Behav Biomed Mater. 2015;52:1-13.

Dingenen JLJ. High performance dyneema fibres in composites. Mat & Des. 1989:10(2):101-4.

Evans FG, Lebow M. Regional differences in some of the physical properties of the human femur. J Appl Physiol 1951;3:563–72.

Flanagan MP, Zikry MA, Wall JW, El-Shiekh A. An Experimental Investigation of High Velocity Impact and Penetration Failure Modes in Textile Composites. 1999;33(12):1080-103.

Fratzl P, Misof K, Zizak I. Fibrillar Structure and Mechanical Properties of Collagen. J Struc Bio. 1997;122:119-22.

Garrano AMC, La Rosa G, Zhang D, Niu LN, Tay FR, Majd H, Arola D. On the mechanical behavior of scales from Cyprinus carpio. J Mechan Behav Biomed Mater 2012;7:17-29.

Greenhalgh ES, Bloodworth VM, Iannucci L, Pope D. Fractographic observations on Dyneema composites under ballistic impact. Comp: Part A. 2013;44:51-62.

Ghods S, Murcia S, Ossa EA, Arola D. Designed for resistance to puncture: The Dynamic Response of Fish Scales. J Mech Behav Biomed Mater. 2017; (in review).

Gil-Duran S, Arola D, Ossa EA. Effect of chemical composition and microstructure on the mechanical behavior of fish scales from Megalops Atlanticus. J Mech Behav Biomed Mater. 2016;56:134-45.

Gilat A, Goldberg RK, Roberts GD. Experimental study of strain-rate-dependent behavior of carbon/epoxy composite. Composites Science and Technology 2002;62(10–1):1469-76.

Grant CA, Brockwell DJ, Radford SE, Thomson NH. Tuning the elastic modulus of hydrated collagen fibrils. Biophy J. 2009;97:2985-92.

Hansen U, Zioupos P, Simpson R, Currey JD, Hynd D. The effect of strain rate on the mechanical properties of human cortical bone. J Biomech Eng. 2008;130(1):011011.

Hsiao HM, Daniel IM. Strain rate behavior of composite materials. Comp Part B: Eng. 1998;29(5):521-33.

Hudspeth M, Nie X, Chen W. Dynamic failure of Dyneema SK76 single fibers under biaxial shear/tension. Poly. 2012;53:5568-74.

Ikoma T, Kobayashi H, Tanaka J, Walsh D, Mann S. Microstructure, mechanical, and biomimetic properties of fish scales from Pagrus major and Oreochromis niloticas. J Struct Bio. 2003;142(3):327-33.

Jacob GC, Starbuck JM, Fellers JF, Simunovic S, Boeman RG. Strain rate effects on the mechanical properties of polymer composite materials. J Appl Poly Sci. 2004;94(1):296–301.

Jandt KD. Biological materials: Fishing for compliance. Nat Mater. 2008;7(9):692-3.

Johnson KL, Trim MW, Francis DK, Whittington WR, Miller JA, Bennett CE, Horstemeyer MF. Moisture, anisotropy, stress state, and strain rate effects on bighorn sheep horn keratin mechanical properties. Acta Biomater. 2017;48:300-8.

Kahler B, Swain MV, Moule A. Fracture-toughening mechanisms responsible for differences in work to fracture of hydrated and dehydrated dentine. J Biomech. 2003;36:229–37.

Karbalaie M, Yazdanirad M, Mirhabibi A. High performance Dyneema fiber laminate for impact resistance/ macro structural composites. J Thermoplastic Comp Mat. 2011;25(4) 403-14.

Kardong KV. Vertebrates: comparative anatomy, function, evolution. Boston (MA): McGraw-Hill; 2006. p. 782.

Khayer Dastjerdi A, Barthelat F. Teleost fish scales amongst the toughest collagenous materials. J Mech Behav Biomed Mater. 2015;52:95-107.

Larsen B, Netto K, Aisbett B. The effect of body armor on performance, thermal stress, and exertion: a critical review. Mil Med. 2011;176(11):1265-73.

Li LP, Herzog W. Strain-rate dependence of cartilage stiffness in unconfined compression: the role of fibril reinforcement versus tissue volume change in fluid pressurization. J Biomech. 2004;37(3):375-82.

Lin YS, Wei CT, Olevsky EA, Meyers MA. Mechanical properties and the laminate structure of Arapaima gigas scales. J Mechan Behav Biomed Mater. 2011;4(7):1145-56.

Liu Z, Jiao D, Weng Z, Zhang Z. Water-assisted self-healing and property recovery in a natural dermal armor of pangolin scales. J Mech Behav Biomed Mater. 2016;56:23-31.

Lucksanasombool P, Higgs WA, Higgs RJ, Swain MV. Fracture toughness of bovine bone: influence of orientation and storage media. Biomaterials 2001;22:3127–32.

Martini R, Barthelat F. Stretch-and-release fabrication, testing and optimization of a flexible ceramic armor inspired from fish scales. Bioinspir Biomim. 2016;11(6):066001.

Maciel KT, Carvalho RM, Ringle RD, Preston CD, Russell CM, Pashley DH. The effects of acetone, ethanol, HEMA, and air on the stiffness of human decalcified dentin matrix. J Dent Res. 1996;75:1851-8.

Mayer G. New classes of tough composite materials—lessons from natural rigid biological systems. Mater Sci and Eng C 2006; 26(8): 1261-1268.

McElhaney JH. Dynamic response of bone and muscle tissue. J. Appl. Physiol. 1966;21: 1231–1236.

McKittrick J, Chen PY, Tombolato L, Novitskaya EE, Trim MW, Hirata GA, Olevsky EA, Horstemeyer MF, Meyers MA. Energy absorbent natural materials and bioinspired design strategies: a review. Mater Sci Eng C. 2010;30:331-42.

Meyers MA, Chen PY, Lopez MI, Seki Y, Lin AY. Biological materials: a materials science approach. J Mech Behav Biomed Mater. 2011;4(5):626-57.

Meyers MA, Lin Y, Olevsky E, Chen P-Y. Battle in the Amazon: Arapaima versus Piranha. Adv Eng Mater. 2012;14(5):B279–88.

Murcia S. The natural armor of fish: an exploration of a biological composite. University of Washington. 2017.

Murcia S, McConville M, Li G, Ossa A, Arola D. Temperature effects on the fracture resistance of scales from Cyprinus carpio. Acta Biomater. 2015;14:154-63.

Murcia S, Li G, Yahyazadehfar M, Sasser M, Ossa A, Arola D. Effects of polar solvents on the mechanical behavior of fish scales. Mater Sci Eng C. 2016;61:23-31.

Murcia S, Lavoie E, Linley T, Devaraj A, Ossa EA, Arola D. The natural armors of fish: A comparison of the lamination pattern and structure of scales. J Mech Behav Biomed Mater. 2017;73:17-27.

Nagia T, Izumi M, Ishii M. Fish scale collagen. Preparation and patial characterization. Int J Food Sci Tech. 2004;29:239-44.

Naleway SE, Porter MM, McKittrick J, Meyers MA. Structural Design Elements in Biological Materials: Application to Bioinspiration. Adv Mater. 2015;27(37):5455-76.

Nalla RK, Balooch M, Ager JW 3rd, Kruzic JJ, Kinney JH, Ritchie RO. Effects of polar solvents on the fracture resistance of dentin: role of water hydration. Acta Biomater. 2005;1(1):31-43.

Nalla RK, Kinney JH, Tomsia AP, Ritchie RO. Role of alcohol in the fracture resistance of teeth. J Dent Res. 2006;85(11):1022-6

Nguyen LH, Ryan S, Cimpoeru SJ, Mouritz AP, Orifici AC. The effect of target thickness on the ballistic performance of ultra high molecular weight polyethylene composite. Int J Imp Eng. 2015;75:174-83.

Nyman JS, Ni Q, Nicolella DP, Wang X. Measurements of mobile and bound water by nuclear magnetic resonance correlate with mechanical properties of bone. Bone. 2008;42:193-9.

Nyman JS, Gorochow LE, Adam Horch R, Uppuganti S, Zein-Sabatto A, Manhard MK, Does MD. Partial removal of pore and loosely bound water by low-energy drying decreases cortical bone toughness in young and old donors. J Mech Behav Biomed Mater. 2013;22:136–45.

O'Masta MR, Dechpande VS, Wadley HNG. Mechanisms of projectile penetration in Dyneema encapsulated aluminum structure. Int J Imp Eng. 2014;74:16-35.

Pashley DH, Agee KA, Carvalho RM, Lee KW, Tay FR, Callison TE. Effects of water and water-free polar solvents on the tensile properties of demineralized dentin. Dent Mater. 2003;19:347-52.

Peleg K, Rivkind A, Aheronson-Daniel L, Isreali Trauma Group. Does Body Armor Protect from Firearm Injuries? J Amer Col Surg. 2006;202(4):643-8.

Ramachandran GN, Chandrasekharan R. Interchain hydrogen bonds via bound water molecules in the collagen triple helix. Biopolymers 1968;6(11):1649-58.

Rudykh S, Ortiz C, Boyce MC. Flexibility and protection by design: imbricated hybrid microstructures of bio-inspired armor. Soft Matter. 2015;11(13):2547-54.

Russell BP, Karthikeyan K, Despande VS, Fleck NA. The high strain rate response of Ultra High Molecular-weight Polyethylene: From fibre to laminate. Int J Imp Eng. 2013;60:1-9.

Ryou H, Pashley DH, Tay FR, Arola D. A characterization of the mechanical behavior of resin-infiltrated dentin using nanoscopic Dynamic Mechanical Analysis. Dent Mater 2013;29(7):719-28.

Sankar S, Sekar S, Mohan R, Rani S, Sundaraseelan J, Sastry T. Preparation and partial characterization of collagen sheet from fish (Lates calcarifer) scales. Int J Biolog Macromol. 2008;42(1):6-9.

Shergold OA, Fleck NA, Radford D. The uniaxial stress versus strain response of pig skin and silicone rubber at low and high strain rates. Int J Impact Eng. 2006;32:1384–402.

Sherman VR, Quan H, Yang W, Ritchie RO, Meyers MA. A comparative study of piscine defense: The scales of Arapaima gigas, Latimeria chalumnae and Atractosteus spatula. J Mech Behav Biomed Mater. 2017;73:1-16.

Sherman VR, Yang W, Meyers MA. The materials science of collagen. J Mech Behav Biomed Mater. 2015;52:22-50.

Sire JY, Huysseune ANN. Formation of dermal skeletal and dental tissues in fish: a comparative and evolutionary approach. Biolog Rev 2003;78(2):219-49.

Song J, Ortiz C, Boyce MC. Threat-protection mechanics of an armored fish. J Mech Behav Biomed Mater. 2011;4(5):699-712.

Sudo S, Tsuyuki K, Ito Y, Ikohagi T. A Study on the Surface Shape of Fish Scales. JSME Int J Ser C. 2002;45(4):1100-5.

Sun CY, Chen PY. Structural design and mechanical behavior of alligator (Alligator mississippiensis) osteoderms. Acta Biomater. 2013;9(11):9049-64.

Torres FG, Troncoso OP, Nakamatsu J, Grande CJ, Gomez CM. Characterization of the nanocomposite laminate structure occurring in fish scales from Arapaima Gigas. Mater Sci Eng C. 2008;28(8):1276-83.

Torres FG, Le Bourhis E, Troncoso OP, Llamoza J. Structure-Property Relationships in Arapaima Gigas Scales Revealed by Nanoindentation Tests. Poly & Poly Comp. 2014;22(4);369-73.

Torres FG, Malásquez M, Troncoso OP. Impact and fracture analysis of fish scales from Arapaima gigas. Mater Sci Eng C. 2015;51:153-7.

Vernerey FJ, Barthelat F. On the mechanics of fishscale structures. Int J Sol Struct 2010;47(17):2268-75.

Verynerey FJ, Musiket K, Barthelat F. Mechanics of fish skin: A computational approch for bio0inspired flecible composites. Int J Sol Struct. 2014;51(1):274-83.

Wang L, Song J, Ortiz C, Boyce MC. Anisotropic Design of a Multilayered Biological Exoskeleton. J Mater Res. 2009;24(12):3477-94.

Wang B, Yang W, Sherman VR, Meyers MA. Pangolin armor: Overlapping, structure, and mechanical properties of the keratinous scales. Acta Biomater. 2016;41:60-74.

Weiner S, Wagner HD. THE MATERIAL BONE: Structure-Mechanical Function Relations. Ann Rev Mater Sci. 1998;28(1):271-98.

Wegst UG, Bai H, Saiz E, Tomsia AP, Ritchie RO. Bioinspired structural materials. Nat Mater. 2015;14(1):23-36.

Wells JM, Rupert NL. Appl XCT for Damage Diagnostics in a B4C Body Armor Plate. Roy Mil Acad. Brussels, Belgium. 2008.

Williams CL, (personal communication), Army Research Labs, Edgewood Maryland.

Yan J, Daga A, Kumar R, Mecholsky JJ. Fracture toughness and work of fracture of hydrated, dehydrated, and ashed bovine bone. J Biomech. 2008;41:1929–36

Yang W, Chen IH, Gludovatz B, Zimmermann EA, Ritchie RO, Meyers MA. Natural flexible dermal armor. Adv Mater 2013a;25(1):31-48.

Yang W, Chen IH, McKittrick J, Meyers MA. Flexible Dermal Armor in Nature. JOM. 2012;64(4):475-85.

Yang W, Gludovatz B, Zimmermann EA, Bale HA, Ritchie RO, Meyers MA. Structure and fracture resistance of alligator gar (Atractosteus spatula) armored fish scales. Acta Biomater 2013b;9(4):5876-89.

Yang W, Sherman V, Gludovatz B, Mackey M, Zimmermann EA, Chang EH, Meyers MA. Protective role of Arapaima gigas fish scales: Structure and mechanical behavior. Acta Biomater. 2014;10(08):3599–614.

Zhang F, Wang A, Li Z, He S, Shao L. Preparation and Characterisation of Collagen from Freshwater Fish Scales. Food Nutr Sci. 2011; 02(08):818-23.

Zhou B, Xu F, Chen CQ, Lu TJ. Strain rate sensitivity of skin tissue under thermomechanical loading. Philos Trans A Math Phys Eng Sci. 2010;368(1912):679-90.

Zhu D, Ortega CF, Motamedi R, Szewciw L, Vernerey F, Barthelat F. Structure and mechanical performance of a “modern” fish scale. Adv Engr Mater. 2012; 14(4):B185-94.

Zhu D, Szewciw L, Vernerey F, Barthelat F. Puncture resistance of the scaled skin from striped bass: collective mechanisms and inspiration for new flexible armor designs. J Mech Behav Biomed Mater 2013;24:30-40.

Zimmermann EA, Gludovatz, B, Schaible, E, Dave NK, Yang W, Meyers MA, Ritchie RO. Mechanical adaptability of the Bouligand-type structure in natural dermal armour. Nat Comm. 2013;4:2634.

Zylberberg DL, Bonaventure J, Cohen-Solal L, Hartmann DJ, Bereiter-Hagn J. Organization and characterization of fibrillar collagens in fish scales in situ and in vitro. J Cell Sci. 1992:103:273-85.

Zylberberg DL, Nicolas G. Ultrastructure of scales in a teleost (Carassius auratus L.) after use of rapid freeze-fixation and freeze-substitution. Cell and Tis Res. 1982;223:349–67.